High-redshift standard candles: predicted cosmological constraints

Anthea L. King,[1,2]★ Tamara M. Davis,[1] K. D. Denney,[2,3]† M. Vestergaard[2,4] and D. Watson[2]

[1]*School of Mathematics and Physics, University of Queensland, Brisbane, QLD 4072, Australia*
[2]*Dark Cosmology Centre, Niels Bohr Institute, University of Copenhagen, Juliane Maries Vej 30, DK-2100 Copenhagen, Denmark*
[3]*Department of Astronomy, The Ohio State University, 140 W. 18th Ave., Columbus, OH 43221, USA*
[4]*Steward Observatory, University of Arizona, 933 North Cherry Avenue, Tucson, AZ 85721*

ABSTRACT

We investigate whether future measurements of high-redshift standard candles will be a powerful probe of dark energy, when compared to other types of planned dark energy measurements. Active galactic nuclei, gamma-ray bursts, and certain types of core collapse supernova have been proposed as potential candidates of such a standard candle. Due to their high luminosity, they can be used to probe unexplored regions in the expansion history of the Universe. Information from these regions can help constrain the properties of dark energy, and in particular, whether it varies over time. We consider both linear and piecewise parameterizations of the dark energy equation of state, $w(z)$, and assess the optimal redshift distribution that a high-redshift standard-candle survey could take to constrain these models. The more general the form of the dark energy equation of state $w(z)$ being tested, the more useful high-redshift standard candles become. For a linear parametrization of $w(z)$, they give only small improvements over planned supernova and baryon acoustic oscillation measurements; a wide redshift range with many low-redshift points is optimal to constrain this linear model. However, to constrain a general, and thus potentially more informative, form of $w(z)$, having many high-redshift standard candles can significantly improve limits on the nature of dark energy, even compared to dark energy experiments currently only in the planning stages.

Key words: quasars: general – cosmological parameters – dark energy.

1 INTRODUCTION

Cosmological measurements suggest that 'dark energy' is the dominant energy component of the Universe, accounting for approximately 70 per cent of the energy density at the present day (e.g. Blake et al. 2011a, 2011b; Conley et al. 2011; Anderson et al. 2012; Padmanabhan et al. 2012; Hinshaw et al. 2013; Planck Collaboration et al. 2013). We have no theory that simultaneously explains both its existence and magnitude, which suggests that the standard model of particle physics, quantum physics, or our theory of gravity are incomplete. The simplest model of dark energy corresponds to Einstein's cosmological constant – a constant energy density, ρ, with negative pressure, p, such that $p = -\rho$, but it could also take a more exotic form such as a dynamical fluid with negative pressure, a scalar potential field, or can be accounted for by a modified theory of gravity such as $f(R)$ (Nojiri & Odintsov 2007). In all models, dark energy can be characterized by its equation of state $w \equiv p/\rho$. Measuring the present value of w and any time variation provides

us with crucial information about the underlying physics of dark energy.

The properties of dark energy can be probed by studying its influence on the expansion of the Universe. Standard candles and rulers are tools for mapping this expansion. Standard candles have had central roles in major cosmological discoveries, from the use of Cepheid variable stars in the discovery of the expanding Universe by Hubble (1929) to the more recent use of Type Ia Supernovae (SNe) in the discovery of the accelerated expansion and 'dark energy' (Riess et al. 1998; Perlmutter et al. 1999).

To investigate the Universe and its expansion, it is important to use data sets from various different probes to break degeneracies between cosmological parameters, and therefore derive tighter constraints (Bahcall et al. 1999; Huterer & Turner 2001; Levine, Schulz & White 2002; Melchiorri et al. 2003; Wang et al. 2004; Mantz et al. 2010). Using multiple probes simultaneously is also important for consistency checks between independent methods and to understand and mitigate systematic errors. Presently, several cosmological probes are being used to study the Universe, including: SNe, baryon acoustic oscillations (BAO), the cosmic microwave background (CMB), weak lensing (WL), and galaxy clustering (CL).

★ E-mail: anthea.king@uqconnect.edu.au
† Marie Curie Fellow.

These probes provide us with important and complementary ways to investigate the properties of dark energy, but at present, with the exception of BAO, all of these methods for making cosmological measurements are restricted to relatively low redshifts. Proposed SN measurements may only be observed out to a redshift of $z < 2.5$ (Grogin et al. 2011; Koekemoer et al. 2011), though the majority of measurements will remain at $z < 1.5$, due to their relative faintness at these redshifts and observational magnitude limits, as well as a decrease in SN rates at high redshifts (Albrecht et al. 2006; Hook 2013). Galaxy surveys [e.g. Sloan Digital Sky Survey (SDSS) (Percival et al. 2010), WiggleZ (Blake et al. 2011a), and Baryon Oscillation Spectroscopic Survey (BOSS) (Anderson et al. 2012)], from which WL, CL, and BAO measurements are made, are also currently restricted to low redshifts ($z \lesssim 1$). Some BAO measurements have been obtained in a higher redshift regime by probing distant galaxies through Lyman-α absorption in quasar spectra (Busca et al. 2013; Slosar et al. 2013). Future galaxy surveys are predicted to extend the redshift range probed by WL and CL to $z \sim 3$ but such surveys will not be completed in the next 5–10 years. With information over a larger redshift range, we can more easily identify time-evolving behaviour in dark energy, if it is present. Fig. 1 shows that a large range of models are all reasonably consistent with the low-redshift data points and become more easily distinguishable with the inclusion of high-redshift measurements.
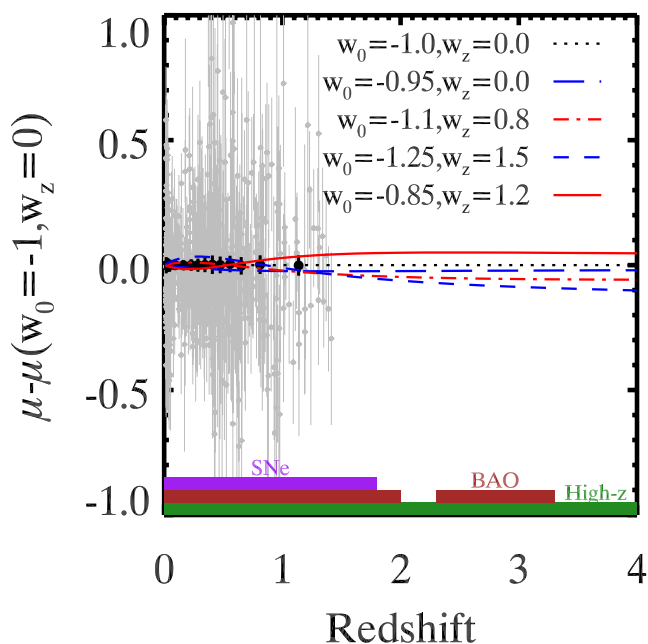
Figure 1. Hubble diagram showing a distance modulus, μ, normalized to that expected for a ΛCDM universe (dotted black curve). Blue and red curves show possible $w(z)$ models. The models of dark energy we show in this figure are described by the Chevallier–Polarski–Linder, CPL, parametrization, $w(z) = w_0 + w_z z/(1 + z)$. ΛCDM is therefore given by $w_0 = 1$; $w_z = 0$. The Union2 SN data (Suzuki et al. 2012) [grey for individual measurements and black for redshift-binned results (Weighted arithmetic mean)] are also shown to demonstrate the range of redshifts currently probed by standard candle measurements. All models shown are hard to distinguish with only these data points. The lines with the same colours represent models that are hard to distinguish with only high-redshift measurements (due to uncertainty in the absolute magnitude) but are easy to distinguish with both high- and low-redshift measurements. The purple, brown, and green shaded regions shown at the bottom of the plot represent the predicted redshift limits of future SN, BAO, and proposed HzSC measurements, respectively.

The models of dark energy we have shown in this figure are described by the Chevallier–Polarski–Linder, CPL, parametrization, $w(z) = w_0 + w_z z/(1 + z)$.

Active galactic nuclei (AGN) have been proposed as high-redshift cosmological probes by Watson et al. (2011) using a technique called reverberation mapping. AGN display a tight empirical radius–luminosity ($r_{BLR}-L(5100\text{Å})$) relation (Koratkar & Gaskell 1991; Wandel, Peterson & Malkan 1999; Kaspi et al. 2000; Bentz et al. 2006, 2009, 2013), which makes them suitable as standardizable candles. Here, r_{BLR} is the distance between the central accretion disc and the broad-emission-line region (BLR), where nebular clouds reprocess the accretion disc continuum radiation of luminosity, L, into emission line photons. The value of r_{BLR} is measured from the observed time lag between the nuclear continuum and broad-emission-line light-curve variations, taken to be the light-travel time between the central source and the BLR (see e.g. Peterson 2001). Since AGN are numerous, highly luminous, and persistent sources of light that are present over a broad range of epochs, they are good candidates for distance measurements. Currently the $r_{BLR}-L$ relationship spans five orders of magnitude in the optical continuum luminosity at 5100 Å from 10^{41} to 10^{46} erg s^{-1} with an observed scatter in the relationship as low as 0.13 dex (equivalent to 0.33 mag in the distance modulus; Bentz et al. 2013), with a clear potential for further reduction in the scatter (Watson et al. 2011) making the relationship a reasonable tool for dark energy investigations.

The $r_{BLR}-L$ relationship is anchored in well-understood photoionization physics (Peterson 1997; Osterbrock & Ferland 2006). AGN broad emission lines are emitted when photoionization equilibrium is attained in the BLR. For systems with the same ionization parameter, gas densities, and ionizing spectral energy distributions (SEDs), this equilibrium occurs at a specific radius. In AGN, at least to the first order, this condition holds, and as a consequence the simple relationship, $r_{BLR} \propto L^{1/2}$, is expected. This $r_{BLR}-L$ relationship can be translated to $\tau/\sqrt{F} \propto D_L$, where τ is the measured time delay ($\tau = r_{BLR}/c$), F is the measured flux of the object, and D_L is the luminosity distance. Thus, a Hubble diagram can be constructed – see fig. 2 of Watson et al. (2011).

The constancy of the ionization parameter, gas densities, and SED between AGN is supported by the agreement between the predicted and observed $r_{BLR}-L$ relationship (Bentz et al. 2009, 2013) and the uniformity in AGN spectra (Vanden Berk et al. 2001, 2004; Dietrich et al. 2002). Despite this, the potential for intrinsic variation in this $r_{BLR}-L$ relationship with black hole characteristics or metallicity, for example, may need to be tested further.

Besides AGN, gamma-ray burst (GRB; Ghirlanda, Ghisellini & Firmani 2006; Speirits, Hendry & Gonzalez 2007; Liang et al. 2008; Diaferio, Ostorero & Cardone 2011; Wei, Wu & Melia 2013), Type II SNe (SNe II; Poznanski, Nugent & Filippenko 2010), and the supernovae associated with gamma-ray bursts (GRB-SNe; Li & Hjorth, in preparation) may also have potential to be standardizable candles, but at this stage, there is no strong evidence to support the use of these probes. New variability surveys make GRBs a highly sought after high-redshift standard candle (HzSC) candidate; however, the physics is still not well known. In contrast, AGN physics is better understood and much of the measurement scatter for AGN can be attributed to known correctable systematics (Watson et al. 2011; Kilerci-Eser et al. in preparation). Accordingly, AGN are likely to be our best candidate at this time.

In our analysis, we determine the requirements for an HzSC to be a competitive cosmological probe regardless of the type of standard candle. We investigate how this general standard candle can complement existing and future constraints on dark energy

properties from Type Ia SNe, BAO, and the CMB. To investigate the properties of dark energy, we consider both a linear, time-evolving dark energy equation of state and a parametrization-independent piecewise equation-of-state model. We also consider how well a general standard candle can measure the Hubble parameter in independent redshift bins, and make an estimate of the dark energy density function. Similar work has been done by Goliath et al. (2001); Huterer & Turner (2001); Frieman et al. (2003); Linder & Huterer (2003) and Salzano et al. (2013) but only with standard candle measurements with the redshift capabilities of SNe and only in conjunction with CMB measurements. We extend the redshift range of the standard candle probe in this case and also consider the inclusion of BAO constraints. Other authors have looked at how future surveys will constrain dark energy but do not consider the possibility of an HzSC (e.g. Albrecht et al. 2006; Sarkar et al. 2008; Eisenstein et al. 2011).

The aim of this paper is to predict the power of standard candle measurements for constraining dark energy properties and determine the optimal redshift distribution required to set the tightest constraints. From this analysis, we can make a judgement about how useful HzSCs are as cosmological probes and define an optimal survey strategy. This paper is organized as follows: Section 2 describes the analysis methods we have implemented, Section 3 outlines the observables and data sets we use, while Section 4 details the parameters we fit. We present the results of our analysis in Section 5. Discussion and conclusions are presented in Section 6.

2 ANALYSIS METHODS

We predict the cosmological information that can be extracted from measurements of a reliable HzSC. In particular, we concentrate on how well an HzSC, with an extended redshift range, can further constrain the properties of dark energy over and above existing and predicted future SN, BAO, and CMB measurements. In order to make these predictions, we employ two different methods.

(i) Parameter fitting (χ^2), and
(ii) Fisher matrix analysis.

The parameter-fitting method uses a χ^2 analysis on mock standard candle data and tests the likelihood of the data given the model. It is the more accurate of the two methods, but can be computationally time consuming. The Fisher matrix method is a second-order Gaussian likelihood estimation that is very popular in predicting the constraints on various cosmological parameters due to its simplicity and speed (e.g. Albrecht et al. 2006; Bassett et al. 2011; More et al. 2013); however, it fails when the errors in the parameter space are non-Gaussian, which is common for individual cosmological probes. Nonetheless, Fisher predictions are reasonably reliable for large numbers of standard candle measurements and for combinations of probes, because as the constraints become tighter, the uncertainties become more Gaussian.

2.1 Parameter fitting (χ^2)

Our first method of analysis is likelihood testing using real data from SN, BAO, and CMB measurements and mock catalogues of standard candle data and future SN and BAO data. The likelihood that the data are consistent with the model is $\mathcal{L} \propto \exp[-\chi^2/2]$. We explore the parameter space using either a grid approach, for simple models (such as the linear dark energy equation-of-state parametrization), or Markov Chain Monte Carlo (MCMC) analysis, for models with many parameters (such as the piecewise parametriza-

tion). We restrict our parameter space to $50.0 \le H_0 \le 100.0$ and $0.15 \le \Omega_m \le 0.4$, where H_0 is the present-day Hubble constant, and Ω_m is the present matter density fraction. Independent measurements of Ω_m (e.g. Samushia et al. 2013) and H_0 (e.g. Sandage et al. 2006; Riess et al. 2011) are consistent with these parameter ranges. For each trial cosmology in our parameter space, picked by MCMC or grid method, we calculate the χ^2 value,

$$\chi^2(\mathcal{P}_{\mathrm{mod}}) = \sum_{ij} \left[x_i^m(\mathcal{P}_{\mathrm{mod}}) - x_i^d \right] C_{ij}^{-1} \left[x_j^m(\mathcal{P}_{\mathrm{mod}}) - x_j^d \right], \qquad (1)$$

where $x_i^m(\mathcal{P}_{\mathrm{mod}})$ is the predicted observable given the model parameters, x_i^d is the observed value, and C_{ij}^{-1} is the inverse covariance matrix of the observable x^d. If the measurements of x^d are independent then the covariance matrix is diagonal, such that $C_{ii} = \sigma_i^2$, where σ_i is the uncertainty in the x_i^d measurement.

If the observable has the form, $x = f(\mathcal{P}) + K$, where K is a constant, and if no prior knowledge of K is assumed at all, we can analytically marginalize over this constant nuisance parameter ($K \in [-\infty, \infty]$). The revised χ^2 equation used for this purpose is given in Appendix A.

2.2 Fisher matrices

The Fisher matrix method is a method of predicting constraints on your parameter space without real or simulated data. It is a second-order approximation of the likelihood. It assumes Gaussian uncertainty on the parameters being fit, as opposed to only Gaussian uncertainties on the measured quantities as in the previous analysis. Using a fiducial model and expected measurement uncertainties, the likelihood in the nearby parameter space is predicted.

The Fisher matrix is defined such that its inverse is the covariance matrix

$$[\mathcal{F}]^{-1} = [C] = \begin{bmatrix} \sigma_\alpha^2 & \sigma_{\alpha\beta} \\ \sigma_{\alpha\beta} & \sigma_\beta^2 \end{bmatrix}, \qquad (2)$$

where σ_α is the uncertainty associated with an arbitrary parameter λ_α, and $\sigma_{\alpha\beta} = \rho \sigma_\alpha \sigma_\beta$, where ρ is known as the correlation coefficient, which varies from 0 (independent) to 1 (completely correlated). Once the Fisher matrix is known, the inverse gives the best possible constraints that we can derive for the parameters given the observed data. According to the Cramer–Rao inequality, the Fisher matrix gives a lower bound on the parameter uncertainty σ in parameter λ_α,

$$\sigma_\alpha \ge \sqrt{\left(F^{-1} \right)_{\alpha\alpha}}. \qquad (3)$$

For N model parameters $\lambda_\alpha, \lambda_\beta, \ldots, \lambda_N$, the Fisher matrix, F, is an $N \times N$ symmetric matrix. Consider b observables, $f_1, f_2, \ldots, f_b$ (such as μ), with which you attempt to measure cosmological parameters, λ_n (such as $\Omega_m, \Omega_\Lambda, w$), where each observable is related to the model parameters by some function, e.g. $\mu = \mu(\Omega_m, \Omega_\Lambda, \ldots)$. Then the elements of the Fisher matrix are given by

$$F_{\alpha\beta} = \sum_b \frac{1}{\sigma_b^2} \frac{\partial f_b}{\partial \lambda_\alpha} \frac{\partial f_b}{\partial \lambda_\beta}, \qquad (4)$$

where each element is summed over the observables. The derivatives of the parameters required for the Fisher matrix analysis are given in Appendix B.

To marginalize over any parameter, the Fisher matrix is inverted, then the associated rows and columns for that parameter are removed from the matrix, and the inverted Fisher matrix is once again inverted to give the revised Fisher matrix. Useful formulae for

performing this marginalization stably are described in the appendix of Matsubara (2004).

Computationally, Fisher matrices are much simpler than performing the full likelihood analysis and is therefore common practice when forecasting the precision of a future survey (Albrecht et al. 2006; Eisenstein et al. 2011).

2.3 Quality measures of constraining power

To quantify the improvement achieved with the addition of a new HzSC, we calculate the predicted change in the constraints of various dark energy parameters. These include the Hubble parameter in several redshift bins $H(z_i)$, a piecewise fit to the dark energy equation of state $w(z_i)$, and a linear parametrization of a time-varying dark energy equation of state, $w(z) = w_0 + w_z z/(1 + z)$. In the latter case, we also consider the figure of merit (FoM) suggested by the Dark Energy Task Force (DETF; Albrecht et al. 2006), given by the inverse of the area within the 95 per cent confidence level (2σ) contours of the parameters w_0 and w_z,

$$\text{FoM} = \frac{1}{\Delta\chi^2 \pi \sqrt{\det \text{Cov}(w_0, w_z)}}, \tag{5}$$

where $\Delta\chi^2 = 6.17$ for two parameters.[1] Despite equation (5) being the definition of the FoM that appears in the DETF report, the more recognizable form of the DETF FoM is given by the expression $[\sigma w_p \times \sigma w_a]^{-1}$, which is equivalent to

$$[\sigma w_p \times \sigma w_a]^{-1} = \frac{1}{\sqrt{\det \text{Cov}(w_0, w_z)}} \approx 19.38 \times \text{FoM}, \tag{6}$$

where $w_p = w(z_p)$ is the dark energy equation-of-state value at the pivot redshift, and the pivot redshift is the redshift at which $w(z)$ has the smallest uncertainty. The transformation between (w_0, w_z) coordinates to (w_p, w_a) coordinates is linear and the Fisher matrix in the (w_p, w_a) variables is $F = M^T F M$, with $\det M = 1$. It follows that the error ellipse in the $w_p - w_a$ plane has the same area as the equivalent ellipse in the $w_0 - w_z$ plane.

We show both values of FoM in our results for simplicity. Throughout our analysis, we assume a flat universe. As a consequence, our results are not directly comparable with those from the DETF, who allowed for curvature. We only consider a flat universe due to the strength of the current constraints on the curvature given by CMB measurements (Planck Collaboration et al. 2013).

3 OBSERVABLES AND DATA

Standard candle measurements provide us with the luminosity distance, D_L, through the relationship between measured flux, F, and intrinsic luminosity. Because F is measured without an absolute luminosity calibration, what is actually calculated from the observables is the distance modulus,

$$\mu = m - M = 5\log[D_L(\mathcal{P}, z)] + \mathcal{M}, \tag{7}$$

where $\mathcal{M} = \log_{10}(c/H_0) + 25$, is a constant over which we marginalize (equation (A1) absorbs the uncertainty in the absolute magnitude, M, as well as the uncertainty in H_0), and $\mathcal{P}$ are the

---

[1] In general, if the likelihood surfaces for all the parameters are Gaussian, any N-dimensional volume is proportional to the square root of the determinant of the covariance matrix of $\{\lambda_i\}$, $\sqrt{\det \text{Cov}(\lambda_1, \lambda_2, \ldots)}$. For $N = 2$, the 1σ or 2σ confidence level contours of the parameters λ_1 and λ_2 are ellipses with the enclosed area given by $\Delta\chi^2 \pi \sqrt{\det \text{Cov}(\lambda_1, \lambda_2)}$, where $\Delta\chi^2$ given by 2.30 or 6.17, respectively (Wang 2008).

parameters that describe the universe and influence the expansion. The luminosity distance, D_L, is given by,

$$D_L = (1 + z)D_M, \tag{8}$$

where z is the redshift and D_M is the comoving tangential distance, defined as

$$D_M = \frac{c}{H_0} \frac{1}{\sqrt{\Omega_k}} \sinh(\sqrt{\Omega_k}\chi) = R_0 \sinh(\sqrt{\Omega_k}\chi), \tag{9}$$

where $R_0 = c/(H_0\sqrt{\Omega_k})$ is the present-day scale factor, and Ω_k is the equivalent energy density fraction of the curvature. The dimensionless comoving distance is,

$$\chi(z) = \int_0^z \frac{H_0}{H(z)} dz \tag{10}$$

The general form of the Hubble parameter, $H(z)$, for a Friedman–Robertson–Walker metric is given by

$$\frac{H(z)^2}{H_0^2} = \Omega_r(1+z)^4 + \Omega_m(1+z)^3 + \Omega_k(1+z)^2$$
$$+ \Omega_x \exp\left\{ 3 \int_0^{1/(1+z)} \frac{dz}{1+z} [1 + w(z)] \right\}, \tag{11}$$

where Ω_r is the current normalized radiation energy density (including the relativistic neutrino density), and Ω_x is the current normalized dark energy density. The energy density is normalized with the critical density, such that $\Omega = \rho/\rho_c$, where ρ_c is the critical energy density of the universe for which the spatial geometry is flat (or Euclidean).

3.1 Data

3.1.1 Existing data

Type Ia supernova: For our analysis, we use the Supernova data from the SuperNova Legacy Survey (SNLS; Conley et al. 2011) which is a compilation of the first three-year results from the SNLS survey with other supernova surveys (Contains: 123 low-z, 93 SDSS, 242 SNLS, and 14 *Hubble Space Telescope* SN measurements). The details of our fitting procedure, including stretch, and colour corrections, are discussed in Appendix C.

Baryon acoustic oscillations: Large-scale structure measurements and consequently BAO measurements can be distilled into simple parameters that can be used to constrain cosmology. Two common parameters are used to express the cosmological information from the BAO measurement: $A(z)$ and d_z. The acoustic parameter, $A(z)$, was introduced by Eisenstein et al. (2005) and is given by

$$A(z) = \frac{D_V(z)\sqrt{\Omega_m H_0^2}}{cz}, \tag{12}$$

where the D_V is the 'dilation scale' distance,

$$D_V(z) = \left(D_M^2 \frac{cz}{H(z)} \right)^{1/3}. \tag{13}$$

The ratio of the sound horizon scale to the dilation scale was given the symbol d_z by Percival et al. (2010),

$$d_z = \frac{r_s(z_d)}{D_V(z)}, \tag{14}$$

Table 1. The BAO distance data set from the 6dFGS, SDSS, WiggleZ, and BOSS surveys.

Survey	z	d_z	$A(z)$
6dFGS	0.106	**0.336 ± 0.015**	0.526 ± 0.028
SDSS	0.2	**0.1905 ± 0.0061**	0.488 ± 0.016
SDSS	0.35	**0.1097 ± 0.0036**	0.484 ± 0.016
WiggleZ	0.44	0.0916 ± 0.0071	**0.474 ± 0.034**
WiggleZ	0.6	0.0726 ± 0.0034	**0.442 ± 0.020**
WiggleZ	0.73	0.0592 ± 0.0032	**0.424 ± 0.021**
BOSS	0.57	**0.0731 ± 0.0018**	–

Notes. Measurements of the distilled parameters d_z and $A(z)$ are quoted. The values in **bold** are the values we have used in our analysis.

where z_d is the redshift at the 'baryon-drag epoch' and $r_s(z_d)$ is the comoving sound horizon at the baryon-drag epoch. The general expression for $r_s(z)$ is given by (Komatsu et al. 2011)

$$r_s(z) = \frac{c}{\sqrt{3}} \int_0^{1/(1+z_d)} \frac{\mathrm{d}a}{a^2 H(a)\sqrt{1 + (3\Omega_b/4\Omega_\gamma)a}}, \tag{15}$$

where $\Omega_\gamma = 2.469 \times 10^{-5}(T_{\mathrm{eff}}/2.725)^4$ is the normalized pure radiation density, a is the normalized scale factor and is related to the redshift by $a^{-1} = 1 + z$, and T_{eff} is the effective temperature of the CMB. We use the fitting formula for z_d defined by Eisenstein & Hu (1998).

The values of these two parameters from Six-degree-Field Galaxy Survey (6dfGS) (Beutler et al. 2011), SDSS (Percival et al. 2010), WiggleZ (Blake et al. 2011b), and BOSS (Anderson et al. 2012) are shown in Table 1.

We use the d_z parameter for our analysis of the 6dfGS, SDSS, and BOSS data and the $A(z)$ parameter when we are considering the WiggleZ data, corresponding to the officially released parameters in the associated papers. These parameters provide the best depiction of the BAO data in each survey. The distilled parameter, $A(z)$, is the most appropriate choice for quantifying the WiggleZ data as it is uncorrelated with $\Omega_m h^2$, but because of the shape of the clustering pattern marginalized over for the 2dfGS, SDSS, and BOSS data, the d_z parameter is the best representation. Therefore, for the χ^2 analysis, we define $x^d = [d_{0.106}[6dfGS], d_{0.2}[SDSS], d_{0.35}[SDSS], A(0.44)[WiggleZ], A(0.6)[WiggleZ], A(0.73)[WiggleZ], d_{0.57}[BOSS]]$, and C_{ij}^{-1} is a 7×7 matrix made up from a combination of the individual errors from the individual measurements from 6dfGS and BOSS and the defined covariance matrices from the WiggleZ (Blake et al. 2011b) and SDSS (Percival et al. 2010) data. We have not included any covariance terms between the surveys, despite the fact that the WiggleZ and SDSS surveys share a sky overlap of 500 square degree for redshift range $z < 0.5$. Given that the SDSS measurement is

derived across an 8000 square degree sky area and the uncertainties in both measurements contain a significant shot noise component, the resulting covariance is negligible (Blake et al. 2011b). We have assumed Gaussian errors in the BAO distances. Non-Gaussian tails may be non-negligible (Percival et al. 2007, 2010; Bassett & Afshordi 2010), but studying their effect is beyond the scope of this paper.

The parameters we consider in the cosmological fitting are $\lambda_\alpha = [\Omega_m, w, H_0, \Omega_b]$. We marginalize over Ω_b and H_0 values after the various probes are combined as the cosmological parameters do not have independent probability distributions.

Cosmic microwave background: We included the CMB data in our cosmological fits using the *Planck* (Planck Collaboration et al. 2013) results. We use the CMB 'distance priors': the shift parameter, $\mathcal{R}$, the acoustic parameter, ℓ_A, and the redshift at the decoupling epoch, z_*. The shift parameter is given by

$$\mathcal{R} = \frac{\sqrt{\Omega_m H_0^2}}{c} D_M(z_*). \tag{16}$$

The acoustic parameter is given by the expression

$$\ell_A = \frac{\pi D_M(z_*)}{r_s(z_*)}, \tag{17}$$

where $r_s(z_*)$ is the sound horizon at recombination. The redshift at photon decoupling is z_* and we implement the Hu & Sugiyama (1996) fitting formula.

The measured *Planck* 'distance priors' (D. Parkinson 2013, private communication) from the Planck Collaboration et al. (2013) are $[\mathcal{R}, \ell_A, z_*] = [1.7440 \pm 0.011, 301.62 \pm 0.19, 1090.02 \pm 0.42]$. These parameters capture most of the constraining power of the CMB data for the dark energy properties (Komatsu et al. 2009). Wang & Wang (2013) published values for $\mathcal{R}$ and ℓ_A from the *Planck* data but did not include a value of z_*. Their findings are consistent with the values stated here.

We again consider the parameters $\lambda_\alpha = [\Omega_m, w, H_0, \Omega_b]$, marginalizing over Ω_b and H_0 values after the various probes are combined.

3.1.2 Mock data

Mock catalogues were constructed to simulate future HzSC measurements (AGN, GRB, SN II) and future SN and BAO measurements. The future SN and BAO predictions are taken from the Stage III and IV predictions from Albrecht et al. (2006). Stage III are intermediate-scale, near-future projects, and Stage IV are large-scale, longer term future projects. Table 2 shows proposed Stage III and IV surveys.

Table 2. Proposed future Stage III and IV cosmological surveys (Yoo & Watanabe 2012). Dark energy projects are classified into four stages: Stage I-completed projects that have already released data, Stage II-on-going projects, Stage III-intermediate-scale, near-future projects, and Stage IV-large-scale, longer-term future projects.

Probes	SN Ia	CMB	BAO	WL
Stage III	DES, Pan-STARRS4, ALPACA, ODI	ALPACA, CCAT	DES, HETDEX, BigBOSS, ALPACA	DES, Pan-STARRS4, ALPACA, ODI
Stage IV	LSST, WFIRST, SNAP, JWST	EPIC, LiteBIRD, B-Pol	LSST, SKA, WFIRST, Euclid, JWST	LSST, SKA, WFIRST, Euclid

References:
ALPACA (Corasaniti et al. 2006), BigBOSS (Schlegel et al. 2011), B-Pol (De Bernardis et al. 2009), CCAT (Radford et al. 2007), DES (Lin 2006), EPIC (Bock et al. 2009), Euclid (Laureijs et al. 2011), HETDEX (Hill et al. 2008), JWST (Gardner 2009), LiteBIRD (Hazumi 2011), LSST (Ivezic et al. 2008), ODI (Jacoby et al. 2002), Pan-STARRS4 (Kaiser 2004), SKA (Torres-Rodríguez & Cress 2007), SNAP (Bebek 2007), WFIRST (Spergel et al. 2013).

Our fiducial model is set as a flat Λ cold dark matter (ΛCDM) universe with the maximum likelihood parameters we determined from the joint SNLS3, SDSS, 6dFGS, WiggleZ, BOSS, and *Planck* constraints, using an MCMC chain with $w = -1$:

    (i) $\Omega_m = 0.30$ (matter energy density),
    (ii) $H_0 = 69.45$ (the Hubble constant),
    (iii) $N_{\rm eff} = 3.04$ (effective number of neutrino-like relativistic degrees of freedom),
    (iv) $T_{\rm eff} = 2.7255$ (effective temperature).

Mock high-z standard candle measurements: a standard candle mock catalogue is constructed by generating perfect distance modulus data according to our fiducial model, and adding random Gaussian error of the order of the predicted scatter.

We generate various mock catalogues for a number of mock surveys varying the redshift range and distribution. We assume, unless specifically mentioned, that the uncertainty in the distance modulus measurement for the standard candle is 0.2 mag, chosen following the expected achievable scatter discussed by Watson et al. (2011) for AGN measurements. We generally consider a large mock standard candle catalogue with 2000 distance measurements. This number was chosen as it is directly comparable to Stage III SN numbers for the individual predicted spectroscopic or photometric surveys. We extend this study to consider AGN distributions and realistic observational restrictions in an upcoming paper.

We have assumed independence between individual standard candle measurements. Correlations could be induced by shared peculiar velocities if close enough to be influenced by the same overdensity (e.g. galaxy cluster) or by lensing magnification if close to the same line of sight. However, our HzSC candidates are typically at a high-enough redshift that peculiar velocity effects are negligible and widely spread enough over the sky that nearby lines of sight are rare, therefore assuming the individual measurements are not correlated is reasonable. As a consequence, the covariance matrix C_{ij} is a diagonal matrix, where $C_{ii} = \sigma_{\mu_i}^2$.

Future SN and BAO constraints: the mock future SN and BAO measurements are also constructed according to our fiducial model with Gaussian scatter. The future BAO and SN predictions are taken from the Stage III and IV predictions from Albrecht et al. (2006).

The predicted SN measurements from DETF (Albrecht et al. 2006) are limited to $z < 1.7$, but future surveys on the *Hubble Space Telescope* and James Webb Space Telescope (JWST) are now expected to observe SNe out to $z < 2.5$ (Grogin et al. 2011; Koekemoer et al. 2011) and possibly $z < 3.5$ (Hook 2013). For consistency with the DETF predictions, we do not include these objects in our future SN predictions. The small number of objects they will find should be considered as part of our predictions for HzSCs. Salzano et al. (2013) have investigated how the high-z SN measurements improve existing SN constraints.

The predicted measurements given by DETF (Albrecht et al. 2006) break the BAO measurement into the perpendicular and transverse components rather than the previously described angle-averaged measurements (d_z and $A(z)$). The predicted DETF BAO constraints are consequently given in terms of $\log(D_M(z))$, and $\log(H(z))$. We follow this prescription in our future BAO predictions. We have used both the ground- and space-based predictions for the BAO and SN predictions. The specifications of the predicted Stage III and IV surveys are described in Table 3. We have chosen an intermediate value for the systematic error values for both the SN and BAO measurements [$\sigma_F = 0.03$ (associated with photo-z uncertainty), $\sigma_{L/Q} = 0.02$ (associated with the linear and quadratic components of z-dependent SN evolution), see Albrecht et al. 2006 for full description] such that the resulting predictions lie directly between the optimistic and pessimistic cases.

We did not consider future CMB constraints at this point as no survey is predicted to supersede Planck, nor will we consider the constraints from WL and clustering measurements, both from redshift surveys and X-ray identification, as it is beyond the scope of this study.

Table 3. The specifications of the predicted Stage III and IV SN and BAO survey measurements.

SNe							
Stage	Type	N	Redshift Range	$\sigma_D{}^a$	$\sigma_F{}^b$	$\sigma_{L/Q}{}^c$	Expected year of completion
III	Spectroscopic	2001	$0.01 < z < 1.0$	0.15	0.00	$0.02/\sqrt{2}$	2017 (HETDEX)
III	Photometric	2001	$0.01 < z < 1.0$	0.12	0.03	$0.02/\sqrt{2}$	2017 (DES)
IV	Spectroscopic	2498	$0.01 < z < 1.7$	0.10	0.00	$0.02/\sqrt{2}$	>2020 (SNAP, WFIRST), 2023 (JWST)
IV	Photometric	191679	$0.01 < z < 1.2$	0.10	0.03	$0.02/\sqrt{2}$	2032 (LSST)
BAO							
Stage	Type	Sky area (deg^2)	Redshift range	$\sigma_F{}^b$			Expected year of completion
III	Spectroscopic	2000	$0.5 < z < 1.3$	0.00			2014 (BOSS), 2017 (HETDEX)
III	Spectroscopic	300	$2.3 < z < 3.3$	0.00			2014 (BOSS)
III	Photometric	4000	$0.5 < z < 1.4$	0.03			2017 (DES)
IV	Spectroscopic	20000	$0.01 < z < 1.5$	0.00			2021 (BigBOSS), >2024 (SKA)
IV	Spectroscopic	10000	$0.5 < z < 2.0$	0.00			2021 (JDEM), 2023 (JWST)
IV	Photometric	20000	$0.2 < z < 3.5$	0.03			2032 (LSST)

^{a}The uncertainty of the corrected apparent magnitudes due solely to variations in the properties of SNe.
^{b}The uncertainty associated with photometrically determined redshifts.
^{c}The uncertainty associated with any redshift dependence in the SN population. The *L* and *Q* stand for the linear and quadratic components of evolution.
References:
HETDEX (HETDEX collaboration 2013), DES (DES collaboration 2014), SNAP/JDEM (Albrecht et al. 2009), WFIRST (National Research Council 2010) LSST (LSST collaboration 2013), BOSS (SDSS-III collaboration 2013), BigBOSS (Dey 2012), JWST (NASA 2014).

4 FITTING PARAMETERS

4.1 Hubble parameter determination

For a flat universe, by transforming the distance modulus into a comoving distance, we can extract an estimate of the Hubble parameter at z through numerical differentiation as

$$H(z) = \frac{1}{c}\left[\frac{\mathrm{d}D_M(z)}{\mathrm{d}z}\right]^{-1}. \tag{18}$$

This technique was proposed by Wang & Tegmark (2005) and allows an independent determination of the Hubble parameter at different redshifts. The Hubble parameter can also be measured through various other techniques, such as BAO measurements and age–redshift relationships. Table D1 in Appendix D shows existing measurements of the Hubble parameter and their associated techniques. For a generic dark energy density evolution, $\rho_x(z)$, the general Hubble parameter formulation given in equation (11) can be simplified to take the form,

$$\frac{H(z)^2}{H_0^2} = \Omega_r(1+z)^4 + \Omega_m(1+z)^3 + \Omega_k(1+z)^2 + \Omega_x\frac{\rho_x(z)}{\rho_x(0)}. \tag{19}$$

Given precise measurements of the current matter density fraction Ω_m, and assuming a flat universe with a relatively negligible current radiation density fraction Ω_r, the dark energy density function, $\rho_x(z)/\rho_x(0)$, can trivially be determined from $H(z)$ at low redshifts. Here, $\rho_x(0)$ is the current dark energy density fraction. We set $\Omega_m = 0.261 \pm 0.037$ as determined from anisotropic clustering of galaxies in the CMASS DR9 (Samushia et al. 2013) in combination with H_0 measurements (Riess et al. 2011), and the full *Wilkinson Microwave Anisotropy Probe* 9 (*WMAP*9) likelihood (Hinshaw et al. 2013) for a w_zCDM model. For our analysis, we broke the SN and HzSC measurements into evenly spaced redshift bins, to match the convention of the Stage III and IV predictions.

4.2 Dark energy equation of state: *w(z)*

All models of dark energy can be characterized by their equation-of-state w, which may evolve with time. Therefore, crucial information about the underlying physics of dark energy can be obtained by measuring the present value of w and any time variation. The two main strategies for investigating the evolution of the dark energy equation of state are to (i) assume a $w(z)$ parametrization and fit to existing data or (ii) determine the value of $w(z)$ in different redshift bins, independent of a dark energy parametrization. The first method can more precisely determine the $w(z)$ behaviour if the parametrization represents the true dark energy evolution. If the dark energy behaves differently than the predicted parametrization, this approach is possibly misleading. The second approach is statistically noisy as it depends on the first and second derivatives of the distance with respect to redshift. A consequence is that the uncertainties on the measurements of $w(z)$ can become substantial. On the other hand, it does not require any a priori assumptions about the properties of the dark energy and, as such, can more easily identify exotic behaviour. We will consider both approaches in our analysis.

4.2.1 Linear w(z) parametrization

We initially consider the linear parametrization of the dark energy equation of state given by the expression

$$w(z) = w_0 + -w_z z/(1+z).$$

This parametrization was first proposed by Chevallier & Polarski (2001) and Linder (2003) and is commonly used throughout the literature.[2] For a cosmological constant (ΛCDM) model, the dark energy equation of state is characterized by $w_0 = -1$ and $w_z = 0$. The dimensionless Hubble parameter for this parametrization is given by

$$\frac{H(z)^2}{H_0^2} = \Omega_r(1+z)^4 + \Omega_m(1+z)^3 + \Omega_k(1+z)^2$$
$$+ \Omega_x(1+z)^{3(1+w_0+w_z)}e^{-3w_z z/(1+z)}. \tag{20}$$

4.2.2 Redshift-binned piecewise w(z)

Next we consider the value of $w(z)$ in different redshift bins, independent of a dark energy parametrization. Under the assumption of general relativity, the dark energy equation of state can be expressed as

$$w(z) = \frac{-(2/3)(1+z)(\frac{\mathrm{d}\chi}{\mathrm{d}z})^{-1}\frac{\mathrm{d}^2\chi}{\mathrm{d}z^2} - 1}{1 - (\frac{\mathrm{d}\chi}{\mathrm{d}z})^2\Omega_m(1+z)^3}, \tag{21}$$

where χ is the dimensionless comoving distance defined earlier (Daly & Djorgovski 2004). Determining this directly in independent redshift bins, through numerical differentiation, as was done for the Hubble parameter in equation (18), is very noisy due to data limitations and the discreteness of the individual measurements. Instead, we consider $w(z)$ as a piecewise function, with a constant equation-of-state parameter within each redshift bin, and fit the parameters $w_1, w_2, \ldots, w_i$ using the Monte Carlo analysis, where w_i is the dark energy equation of state corresponding to the ith redshift bin, z_i. No priors are put on the value of w_i.

By choosing $w(z)$ to be a piecewise constant function (or step function), rather than calculating $w(z)$ directly in each redshift bin as in equation (21), we can fit all the data at once using MCMC and easily incorporate existing SN, BAO, and CMB data, and mock catalogues of future data. This maximizes the information that can be gleaned by the finite number of distance measurements in our samples. However, this process creates correlations in $w(z)$ between the bins, as the distance, $D_M(z)$, requires an integration over 0 to z. The correlations are captured by the covariance matrix, given by $[C] = \langle ww^T\rangle - \langle w\rangle\langle w^T\rangle$. To decorrelate the equation-of-state parameters, we follow the prescription of Huterer & Cooray (2005) and transform the w chains through an orthogonal matrix rotation that diagonalizes the inverse covariance matrix. This is equivalent to applying a weighting function to the correlated w_i values. The new, uncorrelated w_i are given as a linear combination of the correlated w_i described by the weight function.

The dimensionless Hubble parameter in this case is given by the expression

$$\frac{H(z_{N-1} < z \le z_N)^2}{H_0^2} = \Omega_r(1+z)^4 + \Omega_m(1+z)^3 + \Omega_k(1+z)^2$$

$$+ \Omega_x(1+z)^{3(1+w_N)}\prod_{i=0}^{N-1}[1+\max(z_i)]^{3(w_i-w_{i+1})}, \tag{22}$$

where N is the redshift bin where z resides and $\max(z_i)$ is the maximum redshift in the ith redshift bin.

---

[2] This parametrization is equivalent to the common $w(a) = w_0 + (1-a)w_a$, where $w_z = w_a$ but we use the notation w_z as we primarily refer only to redshift in our analysis.

We divide the redshift range into the following five bins: $0.0 \leq z_1 < 0.3$, $0.3 \leq z_2 < 0.8$, $0.8 \leq z_3 < 1.2$, $1.2 \leq z_4 < 4.0$, $4.0 \leq z_5$. The first four bins are constrained by SN, BAO, and HzSC measurements (roughly a low-redshift bin, two medium-redshift bins, and a high-redshift bin), and the highest redshift bin is constrained entirely by CMB measurements, and is therefore largely uncorrelated with the lower redshift bins (i.e. there is no contribution from preceding bins in the weighting function of bin 5). We assume a flat universe and evaluate w_i in each redshift bin i by fitting the data.

5 RESULTS: CONSTRAINTS FROM HIGH-REDSHIFT STANDARD CANDLES

In this section, we quantify the power of standard candle measurements for constraining dark energy properties using the analysis methods described above. Our primary concern is the optimal redshift range for future standard candle measurements.

Defining the optimal redshift range is difficult, as it will depend on the model of w being tested. The redshift range that best constrains a constant w will not be the same as that which best constrains a variable w. In this section, we investigate this multidimensional question and discuss several aspects of the result.

Realistically, the number density of standard candles and the observing capabilities and strategy of a survey will set the number, the measurement uncertainties, and the redshift distribution of standard candle measurements. We consider the effect of observational restrictions on our cosmological predictions, for the specific case of AGN as our standard candle in a forthcoming paper. For the time being, we consider uniform and non-uniform distributions of a general standard candle, spanning a range of redshifts.

For most of our analysis, we keep the number and scatter in our mock HzSC measurements fixed and alter only the redshift distribution. Greater numbers and higher precision will both give monotonic advantages in constraining dark energy. This is obvious from the role of σ in Equations (1) and (4). If we simply assume the main sources of scatter in the standard candle are observational (statistical), rather than intrinsic (systematic), we can

consider the improvement in parameter constraints as a trade-off between the number of measurements and the precision of the measurements. The resulting constraints follow the general relationship $\sigma_\alpha^2 \propto \sigma_\mu^2/N$, where α can represent $(\Omega_m, \Omega_x, w, \dots)$ and σ_μ is the uncertainty in the distance modulus. We illustrate this in Fig. 2 for a flat w_zCDM parametrization and an optimal double Gaussian distribution of standard candle measurements, which we discuss in the next subsection.

5.1 Parameterized models

We consider a CPL dark energy parametrization, as discussed in Section 4.2.1, and initially investigate how the addition of an HzSC affects the likelihood constraints on a flat w_zCDM universe.

We combine the constraints from 2000 mock standard candle measurements, uniformly distributed over a large redshift range $0.01 \leq z \leq 4.0$, with existing and predicted future SN, BAO, and CMB constraints. The resulting Ω_m-w_0 and w_0-w_z confidence contours are shown in Fig. 3. With respect to the current constraints, the introduction of the HzSC measurements makes a marked impact on the precision with which we can determine the matter density and equation-of-state parameters. This improvement is mainly attributed to the large number of measurements (despite the lower precision compared to SNe); however, it is also influenced by the large redshift range of the mock standard candle measurements. Having a larger redshift range predominantly reduces the uncertainty in the w_z parameter. However, when the HzSCs are combined with the predicted future constraints, we find a smaller effect. This is because of the large number and higher precision of predicted future SN data (compared to our mock HzSCs) and the precision and wide redshift range of the predicted future BAO data.

In the Ω_m-w_0 plane, the tilt of the contours is affected by the inclusion of the HzSCs, due to some orthogonality between the probes. As a result, the improvement is more distinguishable than in w_0-w_z, where orthogonality is weak. Consequently, it is difficult to break degeneracies in the equation-of-state parameter using distance probes such as standard candles and standard rulers alone. This degeneracy occurs because w_0 does not appear independently in
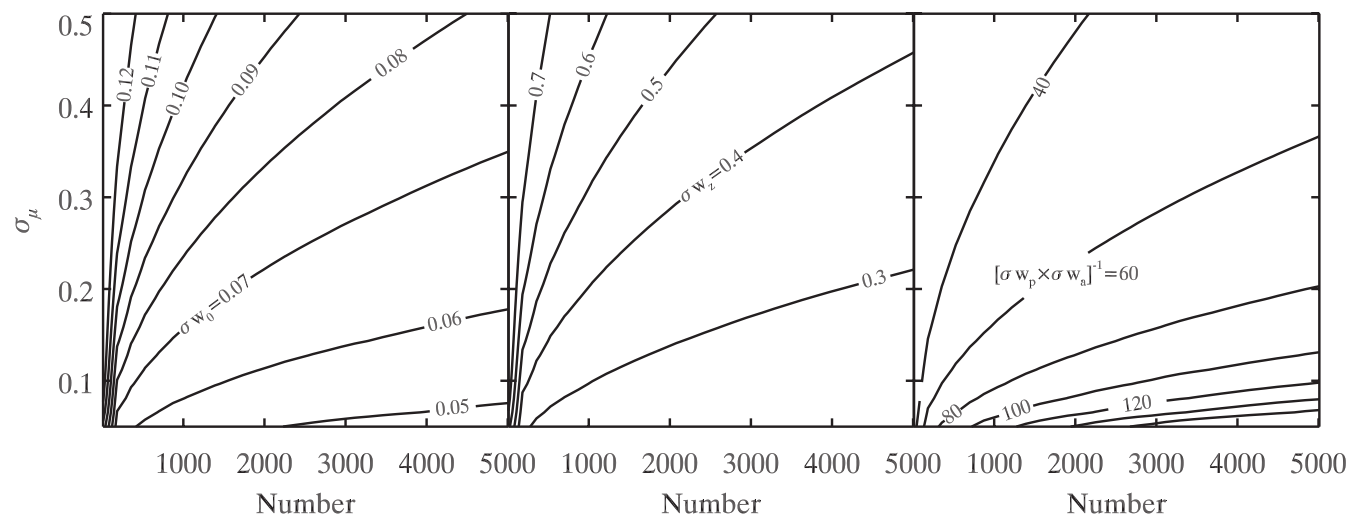
Figure 2. A representation of the trade-off between number of standard candle measurements and the uncertainty in the measurements that dictate the overall dark energy equation-of-state constraints. [Each contour represents a constant absolute uncertainty in w_0 (left) or w_z (middle), or the FoM (right)]. These constraints are calculated with the Fisher matrix methods using the current SN, CMB, and BAO measurements plus additional N standard candles with a double Gaussian distribution with $(\bar{z}_1, \bar{z}_2, \Sigma_1, \Sigma_2) = (0.0, 2.0, 0.25, 0.25)$. The constraints follow the general relationship $\sigma_{w_0, w_z}^2[1/\text{FoM}] \propto \sigma_\mu^2/N$.
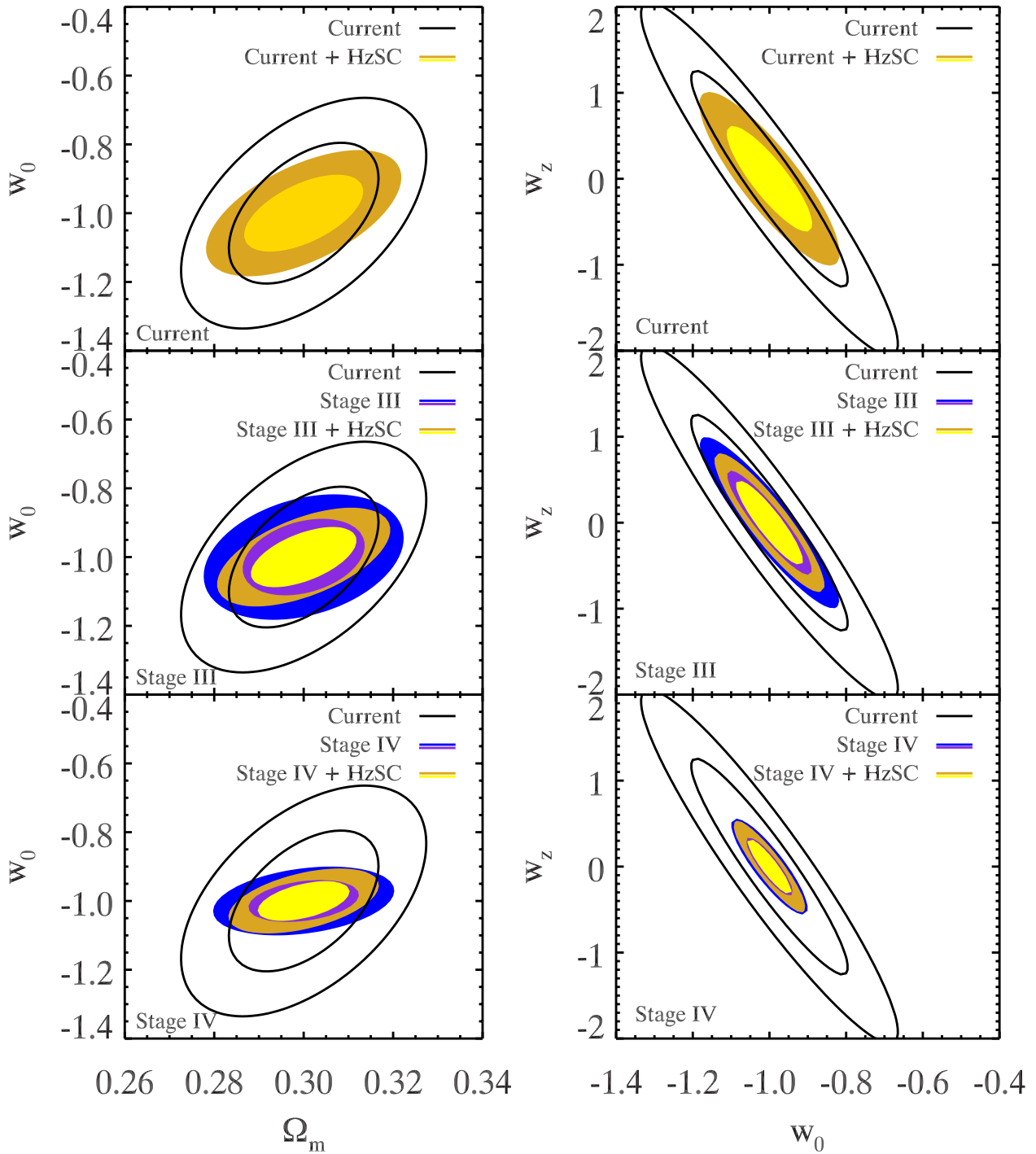
Figure 3. The 1σ and 2σ level confidence contours of the cosmological parameters in the Ω_m-w_0 plane (left) and w_0-w_z plane (right), calculated using Fisher matrix methods. The black contours show the current only SN, BAO, and CMB constraints, the blue/purple contours show the predicted future constraints from Stage III (middle plot) and Stage IV (bottom plot) SN, BAO and CMB data, and the yellow/gold contours in each panel are the combination of those constraints with HzSCs. HzSCs provide significant improvement over current constraints, and are competitive with Stage III probes.

the expression for Hubble parameter. We therefore find that 2000 additional standard candle measurements at high redshift will not improve constraints on this model compared to Stage IV probes, which is not surprising given the relative number of SN and BAO measurements in Stage IV. However, we will see in Section 5.2 that improvements *are* gained when considering more flexible models of dark energy.

This initial investigation is not realistic in the sense that it would be infeasible to carry out an HzSC survey with uniform-redshift sampling and range for this large number of objects, simply because of the realistic number density and redshift distribution of AGNs, SNe II, or GRBs. It also gives us very little information about which redshifts are important for dark energy investigations. In order to inform future HzSC surveys of a more optimal, and possibly more
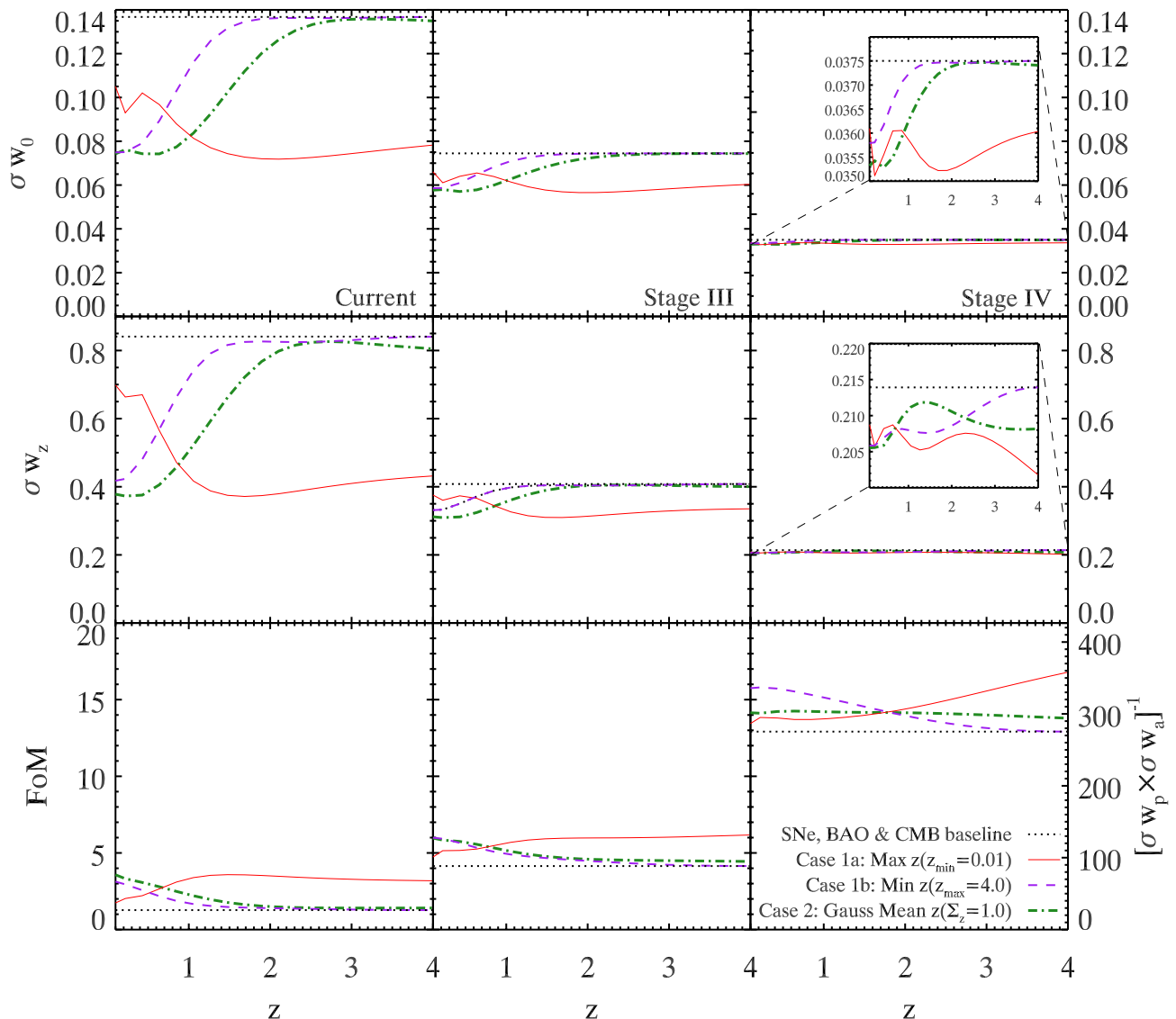
Figure 4. The improvement 2000 standard candles would contribute relative to the dark energy equation-of-state parameter baseline constraints of the combined SN, BAO, and CMB measurements (black curves) based on current data (left-hand plot) and future Stage III (middle plot) and Stage IV (right-hand plot) data, in a flat w_zCDM cosmology. The predicted improvement is shown for the three different HzSC redshift distributions discussed in Section 5.1. The red [solid] [purple (dashed)] curves show results for Case 1a (1b) where the maximum (minimum) redshift is varied for a uniform distribution of standard candles with a fixed minimum (maximum) redshift at $z = 0.01$ ($z = 4.0$). The green (dot–dashed) curves show results for Case 2, where the mean redshift is varied for a Gaussian distribution of standard candles with width $\Sigma_z = 1.0$. Higher FoM values indicate stronger constraints.

realistic, survey strategy, we investigate the constraints on dark energy parameters gained by considering various distributions of HzSCs. To do this, we consider: (1) a uniform-redshift distribution and alter its (a) maximum and (b) minimum redshift cut-offs and (2) a redshift distribution described by a Gaussian function, where the mean and range of redshifts probed is varied by altering the mean and width of the Gaussian function.

5.1.1 Maximum-redshift cut-off (Case 1a)

We set the minimum redshift of our 2000 HzSC measurements to $z_{min} = 0.01$ and varied the maximum redshift, z_{max}, within the range $0.1 \leq z_{max} \leq 4.0$. The HzSC measurements were uniformly distributed in redshift from z_{min} to z_{max}. For each redshift configuration, we calculate the individual w_0 and w_z constraints as well as

the FoM. The resulting constraints are shown by the red solid curves in Fig. 4. In the 'Current' case, where the HzSC measurements are combined with the current data, the constraints initially become stronger as the redshift range increases, but there is a maximum in the FoM at $z_{max} \sim 2$, and beyond this point the constraints weaken. The constraints initially strengthen with redshift as time-evolving behaviour in $w(z)$ becomes easier to identify, and Ω_m constraints tighten with an extended redshift range. The turnover is due to a combination of two effects: (1) a uniform HzSC distribution leads to a relative decrease in the number density of low-z measurements (where dark energy is dominant) as the redshift range is extended; (2) by $z \sim 2$ the energy density of dark energy in the fiducial model is an order of magnitude smaller than the matter energy density, so its influence on the expansion (and measured luminosity distances) is minimal compared to that of the matter density. By increasing

the z_{max} beyond this point, high sensitivity is required to obtain additional information about the dark energy parameters. Overall, the improvement gained with the addition of the HzSCs to Current cosmological probes is primarily due to the large increase in the total number of distance measurements, but the extended redshift range of the HzSCs also reduces degeneracies between w_0 and w_z. The resulting constraints are therefore very dependent on the red-shift distribution of HzSCs. It should be noted here that the CPL dark energy parametrization we investigate was expressly designed as a probe of low-z dynamics, so our results are to some extent a consequence of the parametrization choice.

Once Stage III observations have been completed, SNe and BAO will be competitive with the HzSCs we have simulated here. At that point, the orientation of the constraints, in the w_0-w_z parameter space, start to play a larger role. Different redshift ranges rotate the degeneracy direction in the w_0–w_z plane. In this case, the FoM no longer experiences a turn over and continues to improve with higher z_{max} values. This is a consequence of the other distance probes (SNe and BAO) contributing mostly only at relatively lower redshifts and supports the need for HzSCs, which now complement their lower z counterparts by adding information about the behaviour of dark energy at high z.

By Stage IV, the constraints are already so strong that adding HzSCs gives negligible improvement in the w_0 and w_z constraints. Nonetheless, Fig. 4 shows that the FoM is still improved with the addition of HzSCs at Stage IV because of an increased correlation between the two equation-of-state parameters, thus decreasing the area of the w_0–w_z ellipse without significantly reducing its extent in either parameter.

Despite the fact that 2000 HzSC measurements, with our pre-scribed level of measurement uncertainty, only provide a slight improvement on the combined Stage III and Stage IV measurements in the w_z model, we find that 2000 HzSC measurements are overall competitive as individual probes compared to the individual predicted future SN and BAO measurements. Fig. 5 shows the relative predicted improvement over the current FoM with the individual addition of HzSC measurements, Stage III- and Stage IV-SN and BAO constraints. The HzSC constraints are roughly equivalent to or greater than the predicted Stage III constraints, but to be able to compete with or surpass the Stage IV measurements a large number ($n > 2000$) or more precise measurements ($\sigma_\mu < 0.2$ mag we assumed here) are still required.

We note also that while we have only shown how HzSCs might improve constraints on w_0 and w_z for a flat w_zCDM universe model, we also forecasted the effect on other cosmological parameters. The magnitude of the predicted constraints and the behaviour as a function of z_{max} depends on the cosmological parameter of interest and the parametrization tested. For example, the density parameters (Ω_m, Ω_x) always prefer a long redshift range, which is contrary to what is observed in Fig. 4 for the w_0 and w_z parameters. The complexity of the universe model assumed (e.g. ΛCDM, wCDM, w_zCDM, or different flavours of w_zCDM) also affects the predicted constraints and changes the optimal redshift distribution. Allowing curvature to vary weakens the strength of the dark energy equations-of-state constraints slightly and tends to shift the optimal z_{max} value for w_0 and w_z to a lower redshift. The degradation of the constraints with curvature is expected as there is a well-known degeneracy between dark energy and curvature for purely geometric probes like standard candles (Linder 2005; Knox, Song & Zhan 2006; Huang, Wang & Su 2007; Hlozek et al. 2008).
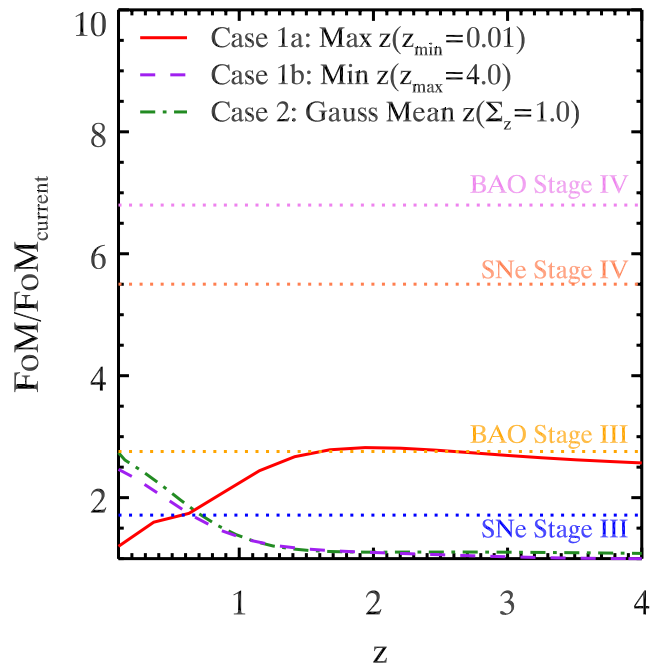

Figure 5. The predicted improvement of the FoM in the w_0−w_z plane in a flat w_zCDM model compared to the current constraints. The non-dotted lines represent the predicted improvement from two uniform distributions with variable maximum (red solid) and minimum (purple dashed) cut-off redshift and one Gaussian distribution with a variable mean redshift (green dot–dashed). These representations are consistent with Fig. 4. The other lines represent the predicted improvement on the current constraints gained with the different stage future experiments. A 2000 large HzSC survey can marginally compete with the Stage IIIs SNe and BAO but cannot compete with either Stage IV SN or BAO predicted constraints.

5.1.2 Minimum-redshift cut-off (Case 1b)

Next, we consider the effect of changing the minimum redshift. We set the maximum redshift to $z_{max} = 4.0$ and vary the minimum redshift within the range $0.01 \leq z_{min} \leq 3.9$. The purple dashed curves in Fig. 4 show that all constraints are maximized when the redshift distribution of HzSCs extends to $z = 0$. The loss of cosmological information as low-redshift data are removed arises not only because dark energy is dominant at low redshifts but also due to uncertainties in the Hubble constant and the absence of an absolute luminosity calibration. In this absence, cosmological information is gained from the shape of the observed Hubble diagram ($d\mu(z)/dz$), rather than the absolute value of $\mu(z)$. Therefore, long redshift ranges are preferred, and high- and low-redshift standard candle information must be on the same absolute magnitude scale in order to robustly probe the evolution of the expansion and minimize systematic uncertainties as a function of z. As a consequence, in the fiducial cosmology, low-redshift standard candle measurements are just as, or more, important as their high-redshift counterparts.

We further illustrate the dependence of the constraints on the redshift, in Fig. 6, by showing how the standard candle-only likeli-hood contours, in the w_0−w_z plane, change with redshift range. We consider three redshift distributions:

(i) $0.01 \leq z \leq 1.0$,
(ii) $0.3 \leq z \leq 4.0$,
(iii) $0.01 \leq z \leq 4.0$.
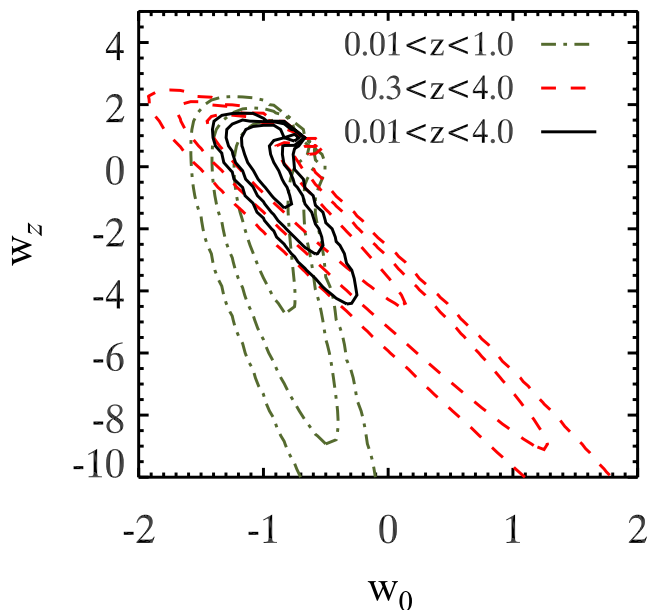
Figure 6. The 1σ, 2σ, and 3σ level confidence contours for three different standard candle survey regimes: (a) $0.01 \leq z \leq 1.0$ (dot–dashed green), (b) $0.3 \leq z \leq 4.0$ (dash red), and (c) $0.01 \leq z \leq 4.0$ (solid black). Current SN and BAO measurements are restricted to $z \lesssim 1$. In this regime, w_0 is well constrained, but to constrain w_z, we clearly require both high- and low-redshift measurements. The likelihoods were calculated using χ^2 analysis as the HzSC-only constraints are not well approximated as Gaussian, unlike the constraints obtained from a combination of all the probes.

When only low redshifts are probed (case i), the w_0 parameter is well constrained, but the w_z parameter is only weakly constrained. At low redshifts, the dynamics of dark energy and consequently the expansion, are predominantly controlled by the value of w_0. On the other hand, probing only high-redshift information (case ii) may be more sensitive to w_z, but without low-redshift constraints, a degeneracy arises between the two equation-of-state parameters and two very different $w(z)$ models may be hard to distinguish. A visual example of this situation is illustrated in Fig. 1, where different models with curves of the same colour appear almost identical at high redshift. Instead, it is optimal to probe a broad redshift range (case iii) to gain tight constraints on w_0 while restricting the possible values of w_z.

Fig. 6 was created using the χ^2 analysis instead of the Fisher matrix analysis, as the Fisher matrix analysis is generally not a good representation of the likelihood of individual probes. See Appendix E for more discussion on this point. The presence of the bend or kink in the contours is primarily due to uncertainties in the matter density (Goliath et al. 2001; Wolz et al. 2012), which cause degeneracies in the w_0 and w_z plane. When standard candle measurements are combined with current CMB and BAO data, this uncertainty diminishes significantly, and the bend disappears.

5.1.3 Single Gaussian distribution (Case 2)

The two previous cases, while instructive, are oversimplified in their assumption of a uniform-redshift distribution of standard candles. Indeed, some redshift ranges may have more power in terms of constraining cosmological parameters (see Fig. 1). Also, uniform-redshift distributions are difficult to achieve in practice due to the small volumes present at low redshift and survey flux limits at larger redshifts even if survey design can attempt to mitigate these effects to some degree.

Here, we consider a Gaussian redshift distribution for our mock HzSC sample. By varying the mean redshift and width of this Gaussian, we can directly probe the relative importance of different redshift regimes in constraining cosmology. We invoke a simple Gaussian distribution with a (variable) mean redshift ($\bar{z}$) and redshift spread (Σ_z), with the number density of standard candle measurements is given by

$$\mathcal{N}(z) = \frac{1}{2\pi\Sigma_z^2} e^{-(z-\bar{z})^2/2\Sigma_z^2}. \tag{23}$$

We initially investigate a constant redshift span by holding the redshift spread Σ_z fixed at $\Sigma_z = 1.0$. This is approximately consistent with a relatively deep flux-limited survey (e.g. 2dF-SDSS LRG and QSO; Croom et al. 2009). The green dot–dashed curves in Fig. 4 show the parameter constraints we compute as a function of $\bar{z}$. The distributions are truncated at zero to avoid unrealistic (negative) redshifts, but the total number of HzSC measurements always remains constant.

In the Current case, the constraints from a Gaussian redshift distribution survey with $\bar{z} = 0$, are optimal and the resulting constraints are directly comparable to those found in the uniformly distributed case with redshift within the range $0.01 < z < 2.0$. This once again solidifies the importance of low-redshift measurements.

In the Stage IV case, the FoM constraints gained from a Gaussian distribution of $\Sigma_z = 1$ are no longer competitive with the strongest uniform distribution configurations, and while there is still a preference for a low mean redshift, it is not as pronounced as it was in the Current and Stage III cases. The low-redshift regime is well constrained by the future SN and BAO measurements, in this case, and broadening the redshift range is now the more efficient approach to constrain dark energy.

When the range of redshifts probed, Σ_z, is also allowed to vary, the constraints do not simply tighten for a decreasing $\bar{z}$ and increasing Σ_z as one may naively expect. Fig. 7 shows that the optimal value of $\bar{z}$ is marginally dependent on our choice of Σ_z. For a narrow survey (i.e. small Σ_z), a small but non-zero $\bar{z}$ is optimal because there are two opposing influences at play: the first, is the preference for low-redshift measurements, and the second, is the preference for a larger redshift range. The relative power of these two preferences depends on the priors imposed. For the current case, where cosmological constraints are relatively weak, only an HzSC survey narrower than $\Sigma_z < 0.5$ will prefer a non-zero $\bar{z}$, while in the Stage III case, the upper width threshold is closer to $\Sigma_z < 0.7$ for a non-zero mean. As our constraints improve with the anticipated Stage III and Stage IV measurements, the preference for a wide redshift range dominates over the need for low-redshift measurements.

5.1.3.1 Double Gaussian: while the global maximum in the FoM shown in Fig. 7 is at low redshifts, it is interesting to note that there is also a small local maximum or plateau in the Current constraints (shown in the inset of Fig. 7). Therefore, information about the dark energy equation-of-state parameter (in the linear parametrization and fiducial model) can be gained from high-redshift data. Due to this, we consider a double Gaussian redshift distribution, $\mathcal{N}(\bar{z}_1, \bar{z}_2, \Sigma_{z(1)}, \Sigma_{z(2)})$, which probes both the high- and low-redshift regimes. As low-redshift data has been found to be of importance, we set one Gaussian distribution to be stationary at a mean redshift of $\bar{z}_1 = 0.0$ with a spread in redshift of $\Sigma_{z(1)} = 0.25$. We then allow the $\bar{z}_2$ and $\Sigma_{z(2)}$ of the second Gaussian distribution to vary. Each distribution contains 1000 measurements. In Fig. 8, the resultant dark energy constraints are shown: in all three cases FoM is maximized when $\Sigma_{z(2)}$ is large. The predicted Current and Stage III case FoM values are both maximized for $1 \leq \bar{z} \leq 2$, while the
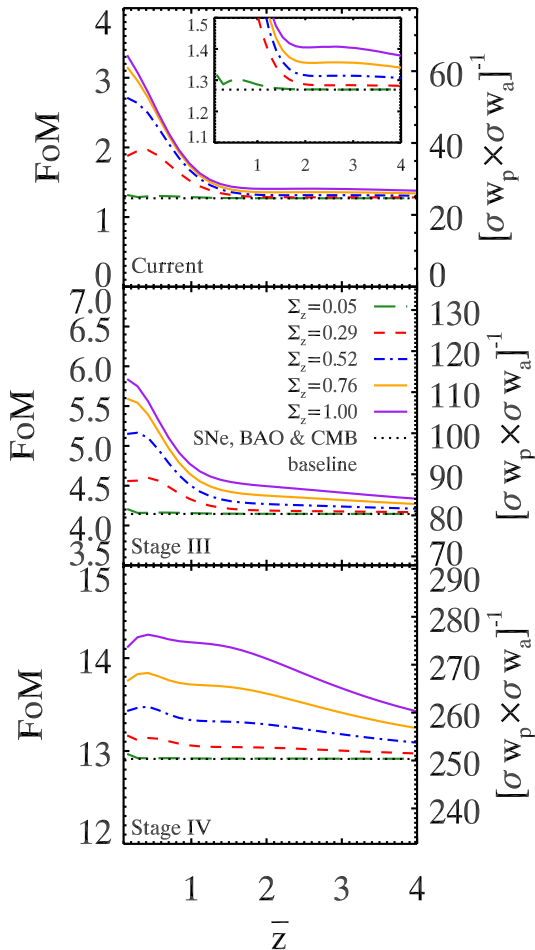
Figure 7. The predicted improvement in the dark energy FoM parameter for 2000 Gaussian distributed HzSCs over the SNe+BAO+CMB baseline (black dotted curves) for Current (top), Stage III (middle), and Stage IV (bottom) constraints, in a w_zCDM cosmology. Coloured curves show the predictions as a function of $\bar{z}$ for a single Gaussian distribution of HzSC measurements with different values of Σ_z. The inset in the top panel shows a zoomed in section of the FoM values.

predicted Stage IV FoM value increases in a roughly monotonic fashion with $\bar{z}_2$. We find that the constraints predicted based on this redshift distribution are marginally superior to the previous distributions tested (Sections 5.1.1 and 5.1.2). This indicates that the optimal redshift regime for an HzSC for a flat w_zCDM model is something like a double Gaussian distribution.

It should be noted that having a double Gaussian distribution of HzSC measurements is different from simply using SN data at low redshift and a different standard candle at high redshift, the low- and high-redshift measurements must be calibrated to the same relative distance scale.

5.1.4 Conclusion

In summary, with only our current SN, BAO, and CMB constraints, the most efficient way of extracting information about dark energy is to focus our observations on the low-z regime but once the Stage III and IV measurements are completed, and constraints tighten, then it is more informative for HzSCs to probe over a longer redshift range.
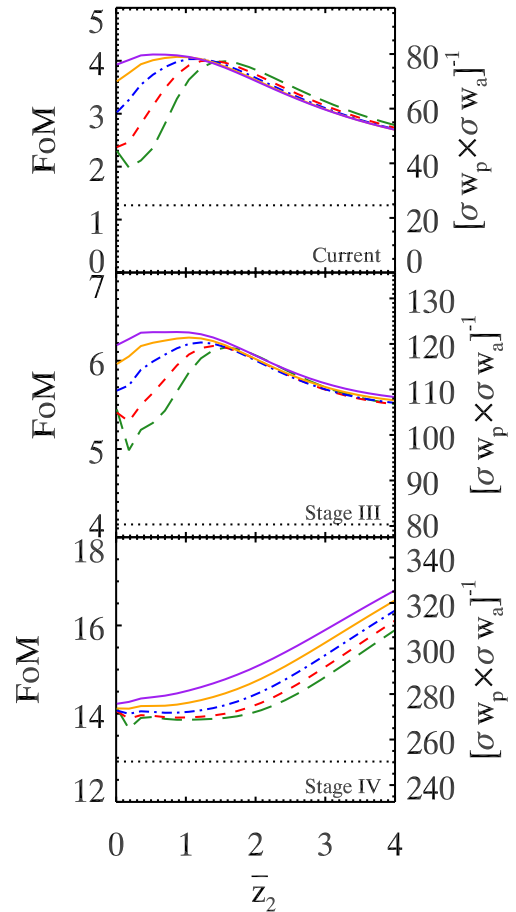
Figure 8. Same as Fig. 7 except the 2000 HzSC measurements are equally split between a stationary Gaussian distribution with $\bar{z}_1 = 0.0$ and $\Sigma_{z(1)} = 0.25$, and a Gaussian distribution with variable redshift mean ($\bar{z}_2$) and spread ($\Sigma_{z(2)}$). Coloured curves represent the same Σ_z magnitudes as Fig. 7 but refer only to changes in $\Sigma_{z(2)}$.

5.2 Piecewise models

5.2.1 Hubble parameter and dark energy density

We applied the numerical derivation technique, described in Section 4.1, to the SNLS SN data,[3] future mock SN measurements, and mock HzSC measurements. The mock HzSC catalogue consists of a uniform distribution of 2000 measurements ranging over $0.01 \leq z \leq 4.0$.

The results are shown in the top panel of Fig. 9 with Hubble parameter measurements from existing BAO data (Blake et al. 2012; Chuang & Wang 2012; Busca et al. 2013), existing differential galaxy age measurements (Simon, Verde & Jimenez 2005; Stern et al. 2010; Moresco et al. 2012; Zhang et al. 2012), and predicted future BAO data. It should be noted that when we refer to the BAO measurement here, we combine the BAO scale with the Alcock & Paczynski effect (Alcock & Paczynski 1979). This effect measures redshift space distortions in the shape of the correlation function or

---

[3] In order to be able to extract the Hubble parameter from the SNLS analysis, we set the stretch and colour parameters as constant, with values $\alpha = 1.45$ and $\beta = 3.16$. These values correspond to the best-fitting values found by Conley et al. (2011) for a flat wCDM model when only considering statistical error.
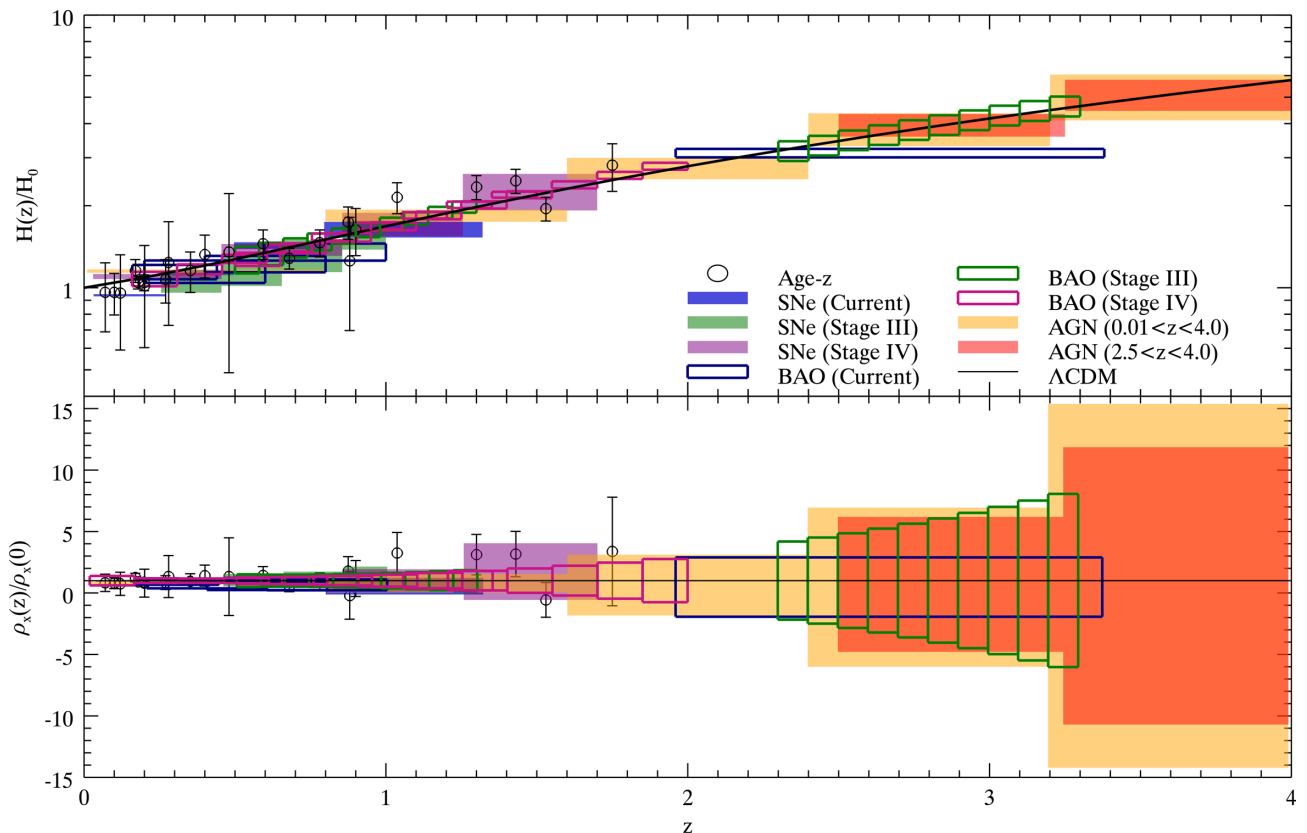
Figure 9. The relative expansion history (Top) and the dark energy density function (Bottom) found in uncorrelated redshift bins from current (blue) and future (green: Stage III, purple: Stage IV) SN (filled) and BAO (open) data, 2000 uniformly distributed simulated HzSC measurement with two redshift ranges $0.01 \leq z \leq 4.0$ (gold-filled) and $2.5 \leq z \leq 4.0$ (orange-filled), and other age-z measurements as listed in Table D1 (black-circle). A fiducial ΛCDM cosmology $(\Omega_m, \Omega_\Lambda, w) = (0.26, 0.74)$ is shown by the black curve. The current data are consistent with our fiducial model. Note that the boxes for the current BAO measurements enclose the full range of redshifts included in each measurement, but the weighted mean is generally offset from the centre of the bin (e.g. the highest redshift current BAO measurement has an effective redshift of 2.3). High redshift measurements will be able to give constraints in the currently unconstrained redshift regime.

power spectrum. It is the combination of these two measurements that gives such precise $H(z)$ measurements. For more details on the existing Hubble parameter measurements see Appendix D. AGN or another HzSC and future BAO measurements will probe the high-redshift regime. The fiducial 2000 HzSC measurements examined here will not be able to compete with the precision of future high-redshift BAO measurements of $H(z)$, per bin, but they can reach somewhat higher redshifts.

As described in Section 4.1, we can also derive the redshift evolution of the dark energy density, $\rho_x(z)/\rho_x(0)$, assuming a flat universe and given a precise measurement of the matter density fraction. The bottom panel of Fig. 9 shows the resulting estimates for the dark energy density function. Current measurements are consistent with $\rho_x(z)/\rho_x(0) = 1.0$ (equivalently, $w = -1$), though the constraints are much weaker in the high-redshift bins. At present, the uncertainty in Ω_m is a dominant source of uncertainty in the dark energy density function estimation, and due to this, an increase in the precision of the Hubble parameter will only provide a relatively small improvement in the overall uncertainty levels of the dark energy density function. Future independent measurements of Ω_m from CL and lensing will help diminish this restriction.

As the dark energy density function measurements are independent of adjacent redshift bins, and depend only on the local $\partial D_m / \partial z$ derivative, we do not require an absolute luminosity calibration or low-redshift measurements to obtain high-redshift information. As

a consequence, we can concentrate our standard candle measurements in the high-redshift regime. For a $2.5 \leq z \leq 4.0$ uniform regime, we can increase the precision on the high-redshift values of $\rho_x(z)/\rho_x(0)$ measurement by about 25 per cent compared to a $0.01 \leq z \leq 4.0$ redshift distribution (orange compared to gold, in Fig. 9). This is simply due to an increase in the number of measurements in this redshift range.

The error bars of the dark energy density function depend on both the number of measurements in each redshift bin, as seen above, and the precision of the measurements. Once again, if we assume the main sources of scatter in the standard candle are statistical, rather than systematic, we can consider the improvement in parameter constraints as a trade-off between the number of measurements and the precision of the measurements. It follows a general $\sigma^2_{H(z)} \propto \sigma^2_\mu / N$ relationship, as observed in the previous section. Therefore, to compete with the predicted future high-redshift Stage III BAO measurements for the dark energy density function, we require either $\sim 20\,000$ HzSC measurements, with $\sigma_\mu = 0.2$ mag or, 2000 HzSC measurements, with $\sigma_\mu \sim 0.06$ mag.

5.2.2 Direct determination of $w(z)$

In Section 4.2.1, we investigated a simple parametrization of the dark energy equation of state and found that depending on the parameter and the complexity of the parametrization the optimal
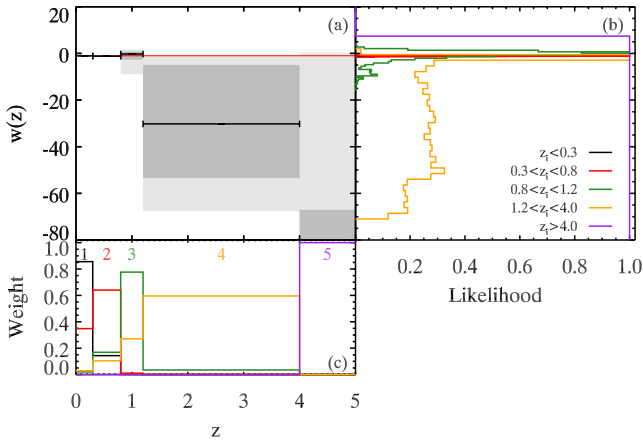
Figure 10. Uncorrelated estimates of the derived piecewise dark energy equation-of-state $w(z_i)$ from current SN, BAO, and CMB data (a). The solid black lines correspond to the median value of $w(z_i)$, the dark and light grey shaded regions correspond to the 68 and 95 per cent confidence levels and the thin red line corresponds to $w(z) = -1$ (ΛCDM). This will form the baseline in which we add our mock HzSC measurements, Stage III and Stage IV constraints. The coloured histograms in panel (b) show the corresponding normalized likelihood histograms for the five redshift bins we consider. Panel (*c*) shows the weighting function which transforms the correlated $w(z_i)$ values into uncorrelated $w(z_i)$ values. The new uncorrelated w_i are given as a linear combination of the correlated w_i described by the weight function. There are no prior constraints on the w_i values.

redshift distribution was variable. Presently, we do not have a strong theory about the true form of dark energy and to properly investigate the potential of HzSC data, we need to consider a more general form of the dark energy. We adopt a general piecewise step function of the equation of state as described in Section 4.2.2 for this purpose, and test how the addition of 2000 uniformly distributed HzSC measurements in the redshift range $0.01 \leq z \leq 4.0$ affects the constraints on the dark energy equation of state in combination with existing SN, BAO, and CMB constraints, compared to the predicted constraints from future surveys.

The derived $w(z_i)$ values for the current SN, BAO, and CMB measurements are shown in Fig. 10. This shows the current status of the field and will act as the base line to which we add our mock HzSC measurements, Stage III, and Stage IV constraints. The lower three redshift bins ($z < 1.2$) are well constrained by the current

data, but beyond $z = 1.2$, the constraints become much weaker. At present, only the CMB measurements and 5 SN measurements contribute to constraining the two highest redshift bins. The current data are consistent with a cosmological constant ($w(z) = -1$). The value of $w(1.2 < z_i < 4.0)$ is also consistent with $w = -1$ and its maximum likelihood values coincide with $w = -1$ (see Panel (b) of Fig. 10 and far right plot Fig. 11), but it remains largely unconstrained for values of $w(z) < -1$. The likelihood displays an almost flat distribution tail. The non-negligible tail in the likelihood curve causes the median value for $w(1.2 < z_i < 4.0)$ to be significantly offset from the maximum likelihood value. To reduce the extent of this tail and make strong constraints on the value of $w(1.2 < z < 4.0)$, we require additional information, for example, HzSC constraints, and/or Stage III and IV constraints. We take a special interest in this redshift range for this reason. Also, despite having the largest redshift range, the last bin is not well constrained, because other parameters, such that Ω_m, H_0, and $\Omega_b h^2$ have a more dominant effect than $w(z > 4.0)$ on the observed CMB parameters. This remains true for all the cases we consider.

The weight functions for each redshift bin are shown in Panel (c) of Fig. 10, where the composition of each redshift bin is distinguished by a different colour (black: $0.0 \leq z_1 < 0.3$, red: $0.3 \leq z_2 < 0.8$, green: $0.8 \leq z_3 < 1.2$, orange: $1.2 \leq z_4 < 4.0$, purple: $4.0 \leq z_5$). As an example, the uncorrelated value of w_i for the lowest redshift bin (black) is a linear combination of $w(z < 0.3)$ ($\sim$85 per cent contribution), $w(0.3 < z < 0.8)$ ($\sim$14 per cent contribution), and $w(0.8 < z < 1.2)$ ($\sim$1 per cent contribution). The $z_5 \geq 4.0$ redshift bin (purple) is predominately constrained by CMB measurements (that is, $z > 4.0$) and, as a consequence, largely uncorrelated with the lower redshift bins. This is apparent in its weighting function, which has no or little contribution from the lower redshift bins. In general our low redshift constraints agree with those found by previous authors (Said et al. 2013; Wang & Dai 2013), but beyond a redshift $z > 0.8$ our constraints were found to be weaker than those found in either Said et al. (2013); Wang & Dai (2013). In both of those studies, independent $H(z)$ measurements and a prior on H_0 were included in their constraints, and the highest redshift bin was held constant at $w_i = -1$. These factors may explain the discrepancy with our results.

Stage III constraints show a marked improvement in the lower three redshift bins over the current constraints. The $w(1.2 < z_i < 4.0)$ is also markedly improved, with the introduction of 10 high-redshift BAO measurements, however, a long distribution tail is still present.
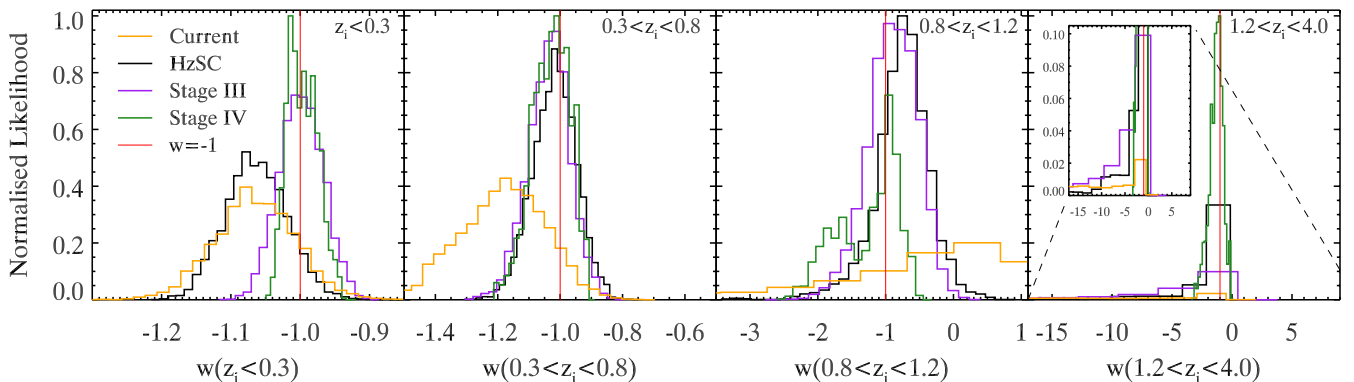
Figure 11. The normalized likelihoods of the uncorrelated $w(z_i)$ values for the Current (orange), $0.01 < z < 4$ HzSC (black), Stage III (purple), and Stage IV (green) constraints, for the four lowest redshift bins (far left: $z_i < 0.3$, middle left: $0.3 < z_i < 0.8$, middle right: $0.8 < z_i < 1.2$, far right: $1.2 < z_i < 4.0$). The thin red line represents $w(z) = -1$. The inset of the far right plot shows a zoomed in section of the likelihood for $w(1.2 < z_i < 4.0)$. We do not show the $z_i > 4.0$ bin because it is poorly constrained.
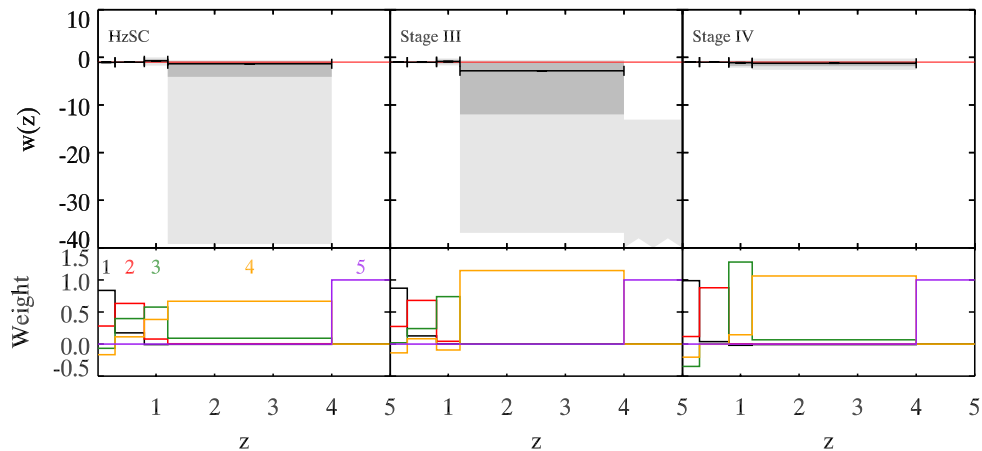
Figure 12. Same as Fig. 10 Panel (a) and (c) but for $0.01 < z < 4.0$ HzSC, Stage III and Stage IV constraints. All these constraints use the current SN, BAO, and CMB measurements as a baseline.

This is evident in the inset of Fig. 11 (Purple). As mentioned, the last redshift bin is again not well constrained, and consequently not shown in the histogram, but with the introduction of the Stage III data an upper limit on the value of $w(z_i > 4.0)$ becomes apparent. The upper limit appears to be approximately $w(z_i > 4.0) < 0.7$ (99.99 per cent upper bound). This upper limit arises because a high value of w corresponds to the dark energy behaving more like matter (when $w > -1/3$ dark energy is attractive), and since we have tight constraints on the matter density and Hubble constant, the data cannot accommodate more matter at early epochs. Therefore, this upper limit represents the value of w for which the dark energy will have a detectable effect on the CMB measurements. However, no lower bound is expected as the lower the value of w, the more negligible the dark energy density is at early times (recall $\Omega(z) \propto [1 + \Delta z]^{3(1+w)}$),[4] and the more negligible is the dark energy's effect on the expansion.

The addition of HzSC measurements to the current constraints considerably strengthens the constraints on $w(1.2 < z_i < 4.0)$ (Fig. 12, left). A slight tail in the likelihood distribution is still present (black curve, Fig. 11), but it has a steeper decline relative to the current and Stage III constraints. As in the Stage III case, an upper limit on $w(z_i > 4)$ is observed of approximately $w(z_i > 4) \lesssim -0.4$ (99.99 per cent upper bound). The presence of this predicted upper limit suggests that both Stage III and HzSC constraints may be able to rule out early time dark energy.

With the introduction of Stage IV constraints, we see significant improvement in all bins (Fig. 12, right). The Stage IV measurements introduce 530 SN and 27 BAO measurements in the $1.2 < z_i < 4.0$ bin, distributed according to Albrecht et al. (2006), and as a consequence can tightly constrain the value of $w(z)$ in this redshift range. It also has the additional advantage of stronger Ω_m, H_0, and Ω_b constraints, which allow the signature of $w(z)$ to be more identifiable.

In the previous section, where we consider a piecewise Hubble parameter and dark energy density function, we introduced a sample of HzSC measurements that only occupied the high-redshift regime and found a marked improvement in the high-redshift constraints. We have used the same technique here with the piecewise $w(z)$ case, with uniformly distributed HzSC measurements over the redshift range $1.2 < z < 4$. The resulting $w(z)$ constraints are shown
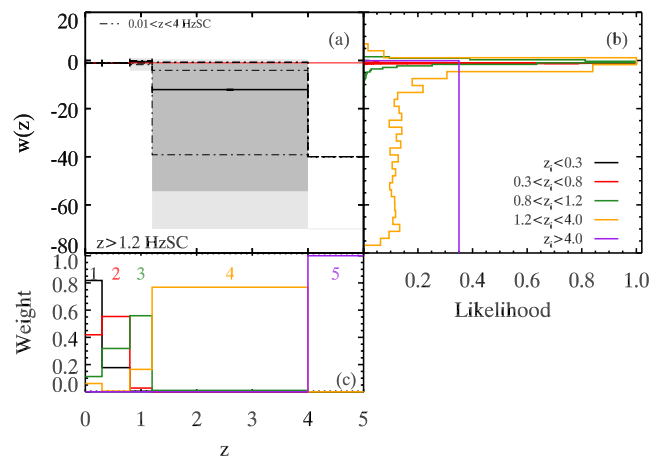
Figure 13. Same as Fig. 10 for the combination of current SN, BAO, and CMB data with 2000 $z > 1.2$ HzSC measurements. In panel (a), we have overlaid the 68 and 95 percentile constrains for the $0.01 < z < 4.0$ HzSC constraints (dot–dashed line).

in Fig. 13. Naively, we would expect to see an improvement in the $w(z_i > 4.0)$ constraints as we saw in the Hubble parameter, but due to the reduced redshift range, the constraints on Ω_m weaken, and correspondingly weaken the $w(z_i > 1.2)$ constraints. Therefore, exclusively obtaining high-redshift measurements is not beneficial for investigating dark energy, when combined with the current constraints, and a full redshift range is optimal. This is analogous to what we find in the linear $w(z)$ parametrization analysis. This did not occur in the dark energy density parameter ($\rho_x(z)/\rho_x(0)$) estimates as the matter density was measured independently.

Finally, we also considered the addition of 2000 uniformly distributed $0.01 < z < 4.0$ HzSC measurements in combination with Stage IV constraints. The resulting $w(z_i)$ values and likelihood curves are shown in Fig. 14. With the addition of the HzSC measurements, the constraints are improved by ~ 30 per cent. This added precision may give new insight into the nature of dark energy and help to cut down the number of allowable dark energy theories.

As we mentioned earlier, in none of the cases was the last bin well constrained. This bin is constrained solely by the CMB data. In some previous studies this last bin was held constant at $w = -1$ (Sullivan, Cooray & Holz 2007; Sarkar et al. 2008; Said et al. 2013;

---

[4] This equation only holds true over a redshift range where w remains constant.
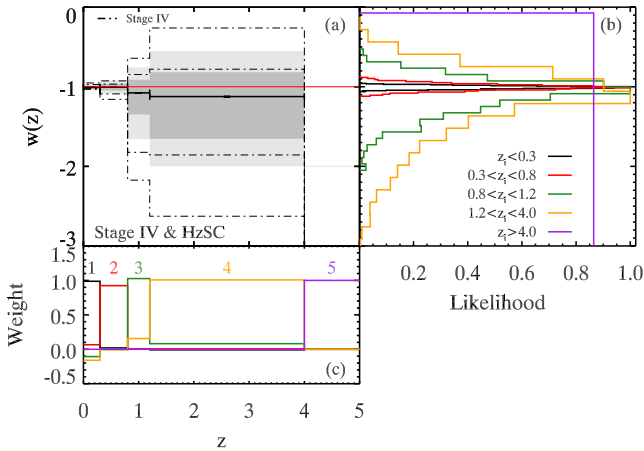
Figure 14. Same as Fig. 10 for Stage IV and $0.01 < z < 4.0$ HzSC constraints. In panel (a) we have overlaid the 68 and 95 percentile constrains for the Stage IV only constraints (dot–dashed line).

Wang & Dai 2013), but we did not want to impose this restriction on our general $w(z)$ expression, as we did not want our data to restrict our model and hinder the revelation of surprises in $w(z)$ if they exist. Despite that, if the low-redshift bins are consistent with $w(z) = -1$, then the dark energy density becomes negligible at high redshifts. As a consequence, determining $w(z)$ beyond this point will require a colossal number of precise distance measurements, and as we saw from our predictions, this may only allow us to determine an upper limit. This prediction is highly dependent on our choice of fiducial model. If we have an underlying varying $w(z)$, it may have a large effect on the expansion of the Universe in the high-redshift regime and be more easily detectable, but current data do not support this hypothesis. In either case, HzSCs are valuable tools for probing these high-redshift regimes, especially in the presence of exotic forms of dark energy.

5.3 Large-scale HzSC survey

So far, we have only considered 2000 HzSC measurements. However, if given the same considerations as Stage IV measurements (e.g. time-scale, cost, and researcher hours), including a dedicated telescope and well-planned observation strategy, it is not unrealistic to consider of the order of 50 000 HzSCs with $\sigma_\mu = 0.2$ or equivalently 12 500 HzSCs with $\sigma_\mu = 0.1$. To investigate the potential of this number of HzSC measurements, we once again consider a flat w_zCDM parametrization of the dark energy equation of state and uniformly distribute the HzSC measurements over the redshift range $0.01 < z < 4.0$. The resulting w_0–w_z probability contours are shown in Fig. 15. The constraints calculated for 50 000 HzSCs measurements (or 12 500 with $\sigma_\mu = 0.1$) are predicted to be comfortably stronger than the predicted combined Stage IV constraints.

The likelihood of this number is strongly dependent on the observational requirements of the proposed HzSC candidate, and while these predictions do not include any systematic errors which can seriously limit the resulting constraints, HzSCs can have a huge potential for exploring the properties of dark energy given sufficient resources.

6 DISCUSSION AND CONCLUSIONS

Our analysis concentrates on the cosmological constraints that can be obtained from any HzSC. We (1) constructed mock standard
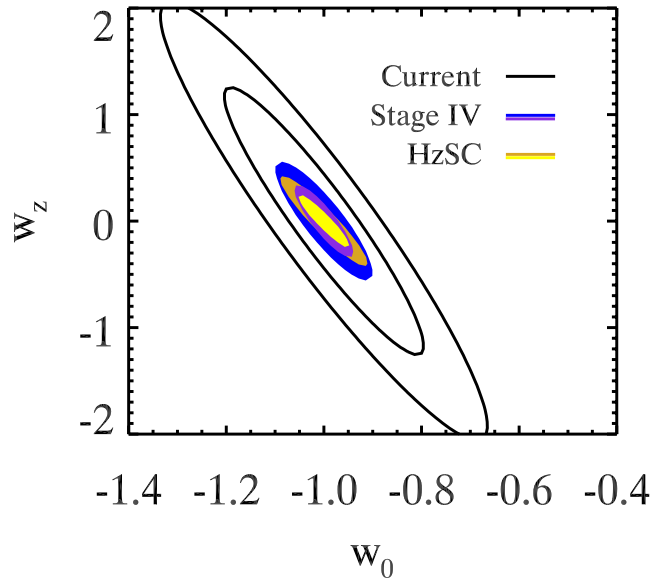
Figure 15. The 1σ and 2σ level confidence contours in the w_0–w_z plane, calculated using the Fisher matrix methods. The black contours show the current SN, BAO, and CMB constraints only, the blue/purple contours show the predicted future constraints from Stage IV SN, BAO, and CMB data, and the yellow/gold contours show the constraints from 50 000 uniformly distributed HzSCs with $\sigma_\mu = 0.2$ or equivalently 12 500 HzSCs with $\sigma_\mu = 0.1$, combined with the current constraints. The predicted constraints from 50 000 (12 500) HzSC measurements exceed the predicted constraints from the joint Stage IV SN and BAO measurements.

candle catalogues with a range of distributions, and (2) using Fisher matrix and χ^2 likelihood analyses, predicted how well HzSC measurements could further constrain the dark energy properties when combined with existing and predicted future SN, BAO, and CMB measurements, and (3) assessed the optimal distribution of HzSC measurements for this type of investigation. Determining whether HzSC measurements could constrain time-evolution in the dark energy equation of state was of primary concern. We approached time-evolution in the equation of state by considering two dark energy models: (1) a linearly parametrized form of the equation of state and (2) a piecewise equation of state.

The HzSCs show their real strength when constraining a general piecewise $w(z)$ parametrization, especially in the so far unconstrained redshift range, $1.2 < z < 4.0$. Even with 2000 HzSC measurements, the constraints in that range from an HzSC uniformly distributed with $0.01 < z < 4.0$ surpass the predicted Stage III constraints, and complement the Stage IV constraints well.

For the linear parametrization case, we generally found that measurement uncertainty, or equivalently the number, and redshift distribution of the HzSCs both have a large effect on the constraints. For a uniform distribution of HzSCs, we observed a general strengthening in the w_0 and w_z constraints when the maximum redshift was increased, especially when combined with the predicted future SN and BAO constraints. Linder & Huterer (2003) found analogous results despite using an alternative dark energy model (i.e. $w = w_0 + w'z$). They also argue that having a long redshift baseline decreases the effects of measurement systematics on the $w(z)$ constraints, which we did not consider. Both ours and Linder's results are dependent on the low-redshift regime being well constrained. The influence of dark energy on the expansion is greatest at low redshifts, so in the absence of low-redshift

measurements, the constraining power of a standard candle is critically diminished.

We determined that a double Gaussian-like distribution was optimal for this type of investigation. This agrees with the results of Frieman et al. (2003), who find the optimal distribution for SN measurements (when combined with CMB measurements) for constraining a linear dark energy equation of state is bimodal, with one population at low redshift and the other above a redshift of 1.0 (although they also use a different parametrization of the equation-of-state parameter). Frieman et al. (2003) restrict their investigation to the low-redshift regime, and did not include BAO measurement prediction. Therefore, our work is able to test the optimal regime for an HzSC in the current state of affairs more robustly.

SNe have been predicted to be observable out to $z < 2.5$ (Grogin et al. 2011; Koekemoer et al. 2011), but the expected number density of SN measurements beyond $z > 1.5$ is low (Albrecht et al. 2006; Hook 2013), and the observed scatter is expected to increase with redshift (Albrecht et al. 2006; Conley et al. 2011). On the other hand, a large number of AGN (87 822 quasars over 3275 deg^2) have been measured between a redshift range $0.058 < z < 5.855$ (SDSS data release 9; Pâris et al. 2012), making either AGN or an equivalent HzSC, potentially the superior distance probes for achieving the optimal distributions in either the uniform or double Gaussian case, and, therefore constraining w_zCDM.

Note that it is not sufficient to combine two different standard candles (for example, strictly HzSC measurements and low-redshift supernovae), unless the two standard candles can be placed on the same relative distance scale. The advantage of a long lever-arm in redshift is negated if the high- and low-redshift populations are distinct, because two different marginalizations over absolute magnitude are required. We gain cosmological information solely from the overall shape of the Hubble diagram and any uncertainty between the scaling of the high- and low-redshift populations affects the accuracy with which the shape can be reconstructed.

However, if we only consider a single Gaussian distribution, a low-redshift mean was preferable and in this redshift regime SNe are likely to be the superior probes of w due to the small observational scatter and minimal observational requirements. In saying that, the strongest $w(z)$ constraints gained from a single Gaussian distribution were found to be weaker than the strongest constraints found for either a uniform or double Gaussian distribution.

The technological requirements and observational resources required to use AGN as cosmological distance indicators are already in place. Given access to the necessary resources, it is a real possibility for the community to obtain the prescribed number of AGN observations contemporaneously with Stage III and well before Stage IV is fully completed.

When combined with the Stage III and Stage IV measurements, 2000 HzSC measurements, with our prescribed level of measurement uncertainty, only provide a slight improvement on the w_zCDM constraints. However, we saw in Fig. 5 that 2000 HzSC constraints are competitive with the individual predicted Stage III SN and BAO constraints. Although 2000 HzSC measurements cannot compete with the individual Stage IV constraints, a 50 000 large HzSC survey with $\sigma_\mu = 0.2$ (or equivalently 12 500 large HzSC survey with $\sigma_\mu = 0.1$) can obtain significantly superior w_0–w_z constraints than the combined SN and BAO Stage IV constraints (Fig. 15). This number is highly optimistic, but depending on the observational requirements of the proposed HzSC, it may be possible to accomplish within the Stage IV timeline. Additionally, a measurement uncertainty of $\sigma_\mu = 0.1$ is feasible to achieve for AGN (Watson et al. 2011, Kilerci-Eser et al. in preparation).

Regardless of the ability for the HzSC to independently constrain dark energy, it will nonetheless act as an independent probe with respect to all other methods, thereby providing a means to more effectively intercalibrate and evaluate systematic uncertainties across the different methods. This is not only a desired but a critical aspect of cosmological distance measurements if we are to constrain the dark energy equation of state.

Interestingly, the amplitude of the measurement uncertainties not only directly affect the constraints that an HzSC can place on all the cosmological parameters, where smaller uncertainties provide stronger constraints. However, they also influence the choice of 'optimal redshift distribution' of the HzSC that can place the best constraints on the dark energy equation-of-state parameters. For example, when considering a double Gaussian distribution, once again anchoring one low-redshift Gaussian with $\bar{z}_1 = 0.0$ and $\Sigma_{z(1)} = 0.25$, and allowing the mean redshift of the second Gaussian to vary, we find that as the scatter is reduced the constraints tighten, as expected, but we also find that the optimal mean redshift tends towards a lower value. This suggests that we could tailor our observation strategy to the quality of the probe.

Caveats: generally, we only consider a flat universe, and though flatness is well supported by observations (Planck Collaboration et al. 2013), this assumption may influence the resulting constraints. We briefly considered the effect of loosening this assumption, and the effects varied depending on the model and parameter of interest. The behaviour of the equation-of-state parameter constraints were not hugely affected by the choice of flatness, though the optimal redshift range was altered slightly.

Throughout our investigations, we assumed a ΛCDM model as our fiducial model to construct our mock catalogues of future measurements. As a consequence, the constraints we derive are affected by this choice. Also we do not consider any source of systematic errors in our predictions, but systematic errors can become a dominant limitation in dark energy investigations. We have not included systematic effects in this investigation, as presently we have insufficient knowledge of the candidate HzSCs to predict the type and magnitude of the possible systematics that may arise. As a consequence, the results of this study are limited by this omission, and represent the most optimistic case. It is crucial for future studies, in which possibly AGN, GRBs, or core collapse SNe are measured, that the systematics are fully investigated.

Gravitational lensing magnification, due to intervening structure along the line of sight, introduces scatter in our luminosity distance measurements and will have a degrading effect on the associated constraints (Holz & Linder 2005). However, rather than just being a source of noise, that adds scatter to the magnitudes, the scatter actually has a specific signature, and measuring the lensing signal in standard candles is an interesting new way to test theories of dark energy, because it measures the effect of the distribution of mass along the line of sight on the paths of the photons (Smith et al. 2014). Therefore, some of the information lost due to the increase in scatter may be gained from studying the lensing signal.

It should be noted that we do not consider modified gravity models in our investigations, so whether high-redshift candles are useful tools in modified gravity models depends on how far the models' predicted expansion history deviates from a flat-ΛCDM model. Other types of measurements, such as growth of structure and cosmic shear, will likely be very useful in distinguishing between such models and standard ΛCDM (Cardone, Camera & Diaferio 2012). Coincidentally, AGNs can also provide extra insight into gravity theory, as reverberation mapping can directly measure the mass of the

central supermassive black hole (Peterson & Horne 2004; Bentz et al. 2009; Denney et al. 2010; Grier et al. 2012; Barth et al. 2013).

Conclusion. HzSCs can be useful in constraining cosmological models, particularly those with a temporally varying dark energy. The number and accuracy needed for standard candle measurements to be competitive with future high-redshift SN and BAO measurements will require significant, long-term observing programs. Nonetheless, seeking to obtain HzSC measurements is a worthwhile enterprise considering (1) the nature of dark energy remains unknown, so gaining additional understanding of it is a significant priority, and (2) there are added benefits of obtaining independent and complementary cosmic distance measurements as a means to further intercalibrate and cross-check current methods. Also, by using AGN as our HzSC, we will help shed light on their nature and on galaxy – black hole co-evolution, since using reverberation mapping methods doubles the use of these measurements, allowing for the mass of the quasar black hole to be measured as well. In a forthcoming paper, we investigate the requirements of a realistic, competitive AGN survey more closely.

REFERENCES

Albrecht A. et al., 2006, preprint (astro-ph/0609591)
Albrecht A. et al., 2009, preprint (arXiv:0901.0721)
Alcock C., Paczynski B., 1979, Nature, 281, 358
Anderson L. et al., 2012, MNRAS, 427, 3435
Bahcall N. A., Ostriker J. P., Perlmutter S., Steinhardt P. J., 1999, Science, 284, 1481
Barth A. J. et al., 2013, ApJ, 769, 128
Bassett B. A., Afshordi N., 2010, preprint (arXiv:1005.1664)
Bassett B. A., Fantaye Y., Hlozek R., Kotze J., 2011, Int. J. Mod. Phys. D, 20, 2559
Bebek C., 2007, Nucl. Instrum. Methods Phys. Res. A, 579, 848
Bentz M. C., Peterson B. M., Pogge R. W., Vestergaard M., Onken C. A., 2006, ApJ, 644, 133
Bentz M. C., Peterson B. M., Netzer H., Pogge R. W., Vestergaard M., 2009, ApJ, 697, 160
Bentz M. C. et al., 2013, ApJ, 767, 149
Beutler F. et al., 2011, MNRAS, 416, 3017
Blake C. et al., 2011a, MNRAS, 415, 2892
Blake C. et al., 2011b, MNRAS, 418, 1707
Blake C. et al., 2012, MNRAS, 425, 405
Bock J. et al., 2009, preprint (arXiv:0906.1188)
Busca N. G. et al., 2013, A&A, 552, A96
Cardone V. F., Camera S., Diaferio A., 2012, J. Cosmol. Astropart. Phys., 2, 30
Chevallier M., Polarski D., 2001, Int. J. Mod. Phys. D, 10, 213
Chuang C.-H., Wang Y., 2012, MNRAS, 426, 226
Conley A. et al., 2011, ApJS, 192, 1
Corasaniti P. S., LoVerde M., Crotts A., Blake C., 2006, MNRAS, 369, 798
Croom S. M. et al., 2009, MNRAS, 392, 19
Daly R. A., Djorgovski S. G., 2004, ApJ, 612, 652
De Bernardis P., Bucher M., Burigana C., Piccirillo L., 2009, Exp. Astron., 23, 5
Denney K. D. et al., 2010, ApJ, 721, 715
DES collaboration, 2014, The Dark Energy Survey, available online at: http://darkenergysurvey.org
Dey A., 2012, An Overview of The Bigboss Project. AAS 219 Metting Jan 2012, available online at: https://bigboss.lbl.gov/trac/attachment/wiki/Public-AAS219Meeting/ArjunDey.pdf
Diaferio A., Ostorero L., Cardone V., 2011, J. Cosmol. Astropart. Phys., 10, 8
Dietrich M., Hamann F., Shields J. C., Constantin A., Vestergaard M., Chaffee F., Foltz C. B., Junkkarinen V. T., 2002, ApJ, 581, 912
Eisenstein D. J., Hu W., 1998, ApJ, 496, 605
Eisenstein D. J. et al., 2005, ApJ, 633, 560
Eisenstein D. J. et al., 2011, AJ, 142, 72
National Research Council, 2010, New Worlds, New Horizons in Astronomy and Astrophysics. The National Academies Press, Washington, DC
Frieman J. A., Huterer D., Linder E. V., Turner M. S., 2003, Phys. Rev. D, 67, 083505
Gardner J. P., 2009, in Onaka T., White G. J., Nakagawa T., Yamamura I., eds, ASP Conf. Ser. Vol. 418, AKARI, a Light to Illuminate the Misty Universe. Astron. Soc. Pac., San Francisco, p. 365
Ghirlanda G., Ghisellini G., Firmani C., 2006, New J. Phys., 8, 123
Goliath M., Amanullah R., Astier P., Goobar A., Pain R., 2001, A&A, 380, 6
Grier C. J. et al., 2012, ApJ, 755, 60
Grogin N. A. et al., 2011, ApJS, 197, 35
Hazumi M., 2011, Prog. Theor. Phys. Suppl., 190, 75
HETDEX collaboration, 2013, Leading the revolution - hetdex, available online at: http://hetdex.org/hetdex/
Hill G. J. et al., 2008, in Kodama T., Yamada T., Aoki K., eds, ASP Conf. Ser. Vol. 399, Panoramic Views of Galaxy Formation and Evolution. Astron. Soc. Pac., San Francisco, p. 115
Hinshaw G. et al., 2013, ApJS, 208, 19
Hlozek R., Cortês M., Clarkson C., Bassett B., 2008, Gen. Relativ. Gravit., 40, 285
Holz D. E., Linder E. V., 2005, ApJ, 631, 678
Hook I. M., 2013, Phil. Trans. R. Soc. A, 371, 20282
Hu W., Sugiyama N., 1996, ApJ, 471, 542
Huang Z.-Y., Wang B., Su R.-K., 2007, Int. J. Mod. Phys. A, 22, 1819
Hubble E., 1929, Proc. Natl. Acad. Sci., 15, 168
Huterer D., Cooray A., 2005, Phys. Rev. D, 71, 023506
Huterer D., Turner M. S., 2001, Phys. Rev. D, 64, 123527
Ivezic Z. et al., 2008, preprint (arXiv:0805.2366)
Jacoby G. H., Tonry J. L., Burke B. E., Claver C. F., Starr B. M., Saha A., Luppino G. A., Harmer C. F. W., 2002, in Tyson J. A., Wolff S., eds, SPIE Conf. Ser., Vol. 4836, Survey and Other Telescope Technologies and Discoveries. SPIE, Bellingham, p. 217
Kaiser N., 2004, in Oschmann J. M., Jr, ed., SPIE Conf. Ser., Vol. 5489, Ground-based Telescopes, SPIE, Bellingham, p. 11
Kaspi S., Smith P. S., Netzer H., Maoz D., Jannuzi B. T., Giveon U., 2000, ApJ, 533, 631
Khedekar S., Majumdar S., 2013, J. Cosmol. Astropart. Phys., 2, 30
Knox L., Song Y.-S., Zhan H., 2006, ApJ, 652, 857
Koekemoer A. M. et al., 2011, ApJS, 197, 36

Komatsu E. et al., 2009, ApJS, 180, 330
Komatsu E. et al., 2011, ApJS, 192, 18
Koratkar A. P., Gaskell C. M., 1991, ApJ, 370, L61
Laureijs R. et al., 2011, preprint (arXiv:1110.3193)
Levine E. S., Schulz A. E., White M., 2002, ApJ, 577, 569
Liang N., Xiao W. K., Liu Y., Zhang S. N., 2008, ApJ, 685, 354
Lin H., 2006, in Barnes P. D., Cooper M. D., Eisenstein R. A., van Hecke H., Stephenson G. J., eds, AIP Conf. Ser., Vol. 842, Particles and Nuclei. Am. Inst. Phys., New York, p. 989
Linder E. V., 2003, Phys. Rev. Lett., 90, 091301
Linder E. V., 2005, Astropart. Phys., 24, 391
Linder E. V., Huterer D., 2003, Phys. Rev. D, 67, 081303
LSST collaboration, 2013, Lsst Timeline, available online at: http://www.lsst.org/lsst/science/timeline
Mantz A., Allen S. W., Rapetti D., Ebeling H., 2010, MNRAS, 406, 1759
Matsubara T., 2004, ApJ, 615, 573
Melchiorri A., Bode P., Bahcall N. A., Silk J., 2003, ApJ, 586, L1
More S., van den Bosch F. C., Cacciato M., More A., Mo H., Yang X., 2013, MNRAS, 430, 747
Moresco M. et al., 2012, J. Cosmol. Astropart. Phys., 8, 6
NASA, 2014, JWST Vital Statistics, available oneline at: http://jwst.nasa.gov/facts.html
Nojiri S., Odintsov S. D., 2007, J. Phys. Conf. Ser., 66, 012005
Osterbrock D. E., Ferland G. J., 2006, Astrophysics of Gaseous Nebulae and Active Galactic Nuclei, 2nd edn, University Science Books, Mill Valley, CA
Padmanabhan N., Xu X., Eisenstein D. J., Scalzo R., Cuesta A. J., Mehta K. T., Kazin E., 2012, MNRAS, 427, 2132
Pâris I. et al., 2012, A&A, 548, A66
Percival W. J., Cole S., Eisenstein D. J., Nichol R. C., Peacock J. A., Pope A. C., Szalay A. S., 2007, MNRAS, 381, 1053
Percival W. J. et al., 2010, MNRAS, 401, 2148
Perlmutter S. et al., 1999, ApJ, 517, 565
Peterson B. M., 1997, An Introduction to Active Galactic Nuclei. Cambridge Univ. Press, Cambridge
Peterson B. M., 2001, in Aretxaga I., Kunth D., Mújica R., eds, Advanced Lectures on the Starburst-AGN. World Scientific Press, Singapore, p. 3
Peterson B. M., Horne K., 2004, Astron. Nachr., 325, 248
Planck Collaboration et al., 2013, preprint (arXiv:1303.5076)
Poznanski D., Nugent P. E., Filippenko A. V., 2010, ApJ, 721, 956
Radford S. J. E., Giovanelli R., Sebring T. A., Zmuidzinas J., 2007, in Karpov A., ed., Eighteenth International Symposium on Space Terahertz Technology. Air and Waste Management Association, p. 32
Riess A. G. et al., 1998, AJ, 116, 1009
Riess A. G. et al., 2011, ApJ, 730, 119
Said N., Baccigalupi C., Martinelli M., Melchiorri A., Silvestri A., 2013, Phys. Rev. D, 88, 043515
Salzano V., Rodney S. A., Sendra I., Lazkoz R., Riess A. G., Postman M., Broadhurst T., Coe D., 2013, A&A, 557, A64
Samushia L. et al., 2013, MNRAS, 429, 1514
Sandage A., Tammann G. A., Saha A., Reindl B., Macchetto F. D., Panagia N., 2006, ApJ, 653, 843
Sarkar D., Sullivan S., Joudaki S., Amblard A., Holz D. E., Cooray A., 2008, Phys. Rev. Lett., 100, 241302
Schlegel D. et al., 2011, preprint (arXiv:1106.1706)
SDSS-III collaboration, 2013, BOSS: Dark Energy and the Geometry of Space, available online at: http://www.sdss3.org/surveys/boss.php
Simon J., Verde L., Jimenez R., 2005, Phys. Rev. D, 71, 123001
Slosar A. et al., 2013, J. Cosmol. Astropart. Phys., 4, 26
Smith M. et al., 2014, ApJ, 780, 24
Speirits F. C., Hendry M. A., Gonzalez A., 2007, Phil. Trans. R. Soc. A, 365, 1395
Spergel D. et al., 2013, preprint (arxiv:1305.5422)
Stern D., Jimenez R., Verde L., Kamionkowski M., Stanford S. A., 2010, J. Cosmol. Astropart. Phys., 2, 8
Sullivan S., Cooray A., Holz D. E., 2007, J. Cosmol. Astropart. Phys., 9, 4
Suzuki N. et al., 2012, ApJ, 746, 85
Torres-Rodríguez A., Cress C. M., 2007, MNRAS, 376, 1831

Vanden Berk D. E. et al., 2001, AJ, 122, 549
Vanden Berk D., Yip C., Connolly A., Jester S., Stoughton C., 2004, in Richards G. T., Hall P. B., eds, ASP Conf. Ser. Vol. 311, AGN Physics with the Sloan Digital Sky Survey. Astron. Soc. Pac., San Francisco, p. 21
Wandel A., Peterson B. M., Malkan M. A., 1999, ApJ, 526, 579
Wang Y., 2008, Phys. Rev. D, 77, 123525
Wang F. Y., Dai Z. G., 2013, Phys. Rev. D., 89, 023004
Wang Y., Tegmark M., 2005, Phys. Rev. D, 71, 103513
Wang Y., Wang S., 2013, Phys. Rev. D, 88, 043522
Wang S., Khoury J., Haiman Z., May M., 2004, Phys. Rev. D, 70, 123008
Watson D., Denney K. D., Vestergaard M., Davis T. M., 2011, ApJ, 740, L49
Wei J.-J., Wu X.-F., Melia F., 2013, ApJ, 772, 43
Wolz L., Kilbinger M., Weller J., Giannantonio T., 2012, J. Cosmol. Astropart. Phys., 9, 9
Yoo J., Watanabe Y., 2012, Int. J. Mod. Phys. D, 21, 30002
Zhang C., Zhang H., Yuan S., Zhang T.-J., Sun Y.-C., 2012, preprint (arXiv:1207.4541)

APPENDIX A: ANALYTICAL MARGINALIZATION OF CONSTANT

If an observable has the form, $x = f(\mathcal{P}) + K$, where K is a constant, and if no prior knowledge of K is assumed at all, the general χ^2 function (equation 1) can be integrated analytically over ($K \in [-\infty, \infty]$). The resulting revised $\bar{\chi}^2$ equation is then given by the expression (Goliath et al. 2001; Conley et al. 2011)

$$\bar{\chi}^2 = A - \frac{B^2}{C}, \tag{A1}$$

where A is equivalent to original χ^2 equation

$$A = \sum_{ij} \left[x_i^m(\mathcal{P}_{\mathrm{mod}}) - x_i^d \right] C_{ij}^{-1} \left[x_j^m(\mathcal{P}_{\mathrm{mod}}) - x_j^d \right], \tag{A2}$$

and

$$B = \sum_{i} \left[x_i^m(\mathcal{P}_{\mathrm{mod}}) - x_i^d \right] C_{ii}^{-1},$$

$$C = \sum_{ij} C_{ii}^{-1}.$$

APPENDIX B: MATHEMATICS FOR FISHER MATRIX CALCULATIONS

The Fisher matrix is formally defined as the expectation value of the derivatives of the log of the likelihood with respect to the parameter λ

$$F_{\alpha\beta} = -\left\langle \frac{\partial^2 \ln \mathcal{L}}{\partial \lambda_\alpha \partial \lambda_\beta} \right\rangle, \tag{B1}$$

or more simply the second derivative of χ^2 centred on the best-fitting value. This comes from the Taylor expansion of χ^2 (corresponding to the likelihood function) around the best-fitting value. Because the best-fitting value corresponds to a minimum in χ^2 (i.e. $d\chi^2/d\lambda|_{\lambda_0} = 0$), the second order term, $d^2\chi^2/d\lambda^2|_{\lambda_0}$, becomes the most important term. Comparing these two definitions of the Fisher matrix, we can recover the general χ^2 equation, which includes the correlation coefficient, ρ,

$$\chi^2 = \frac{\left(\frac{\Delta x}{\sigma_x}\right)^2 + \left(\frac{\Delta y}{\sigma_y}\right)^2 - 2\rho \left(\frac{\Delta x}{\sigma_x}\right) \left(\frac{\Delta y}{\sigma_y}\right)}{1 - \rho^2}. \tag{B2}$$

For the analysis of SNe and HzSCs, our two observables are z and μ, and the error in redshift is negligible, so the elements of the Fisher matrix for this analysis are

$$F_{\alpha\beta} = \sum_z \frac{1}{\sigma_\mu^2} \frac{\partial \mu(z)}{\partial \lambda_\alpha} \frac{\partial \mu(z)}{\partial \lambda_\beta}. \tag{B3}$$

We define a new parameter $\mathcal{E} = H^2(z)/H_0^2 = E^2(z)$, such that

$$\frac{\partial \mathcal{E}}{\partial \Omega_m} = (1+z)^3 - b(z), \tag{B4}$$

$$\frac{\partial \mathcal{E}}{\partial \Omega_x} = f(z) - b(z), \tag{B5}$$

$$\frac{\partial \mathcal{E}}{\partial w} = \Omega_x \frac{\partial f(z)}{\partial w}. \tag{B6}$$

where $b(z) = (1+z)^2$, which corresponds to the curvature term and is included, as Ω_k is dependent on the values of Ω_m and Ω_x, such that $\Omega_k = 1 - \Omega_m - \Omega_x$. Also $f(z) = (1+z)^{3(1+w_0+w_z)} e^{-3w_z z/(1+z)}$.

For the linear (CPL) parametrization of dark energy, $w(z) = w_0 + w_z z/(1+z)$,

$$\frac{\partial \mathcal{E}}{\partial w_0} = \Omega_x \frac{\partial f(z)}{\partial w_0} \tag{B7}$$

$$= 3\Omega_x f(z) \ln(1+z), \tag{B8}$$

and

$$\frac{\partial \mathcal{E}}{\partial w_z} = \Omega_x \frac{\partial f(z)}{\partial w_z} \tag{B9}$$

$$= 3\Omega_x f(z) \left(\ln(1+z) - \frac{z}{1+z} \right). \tag{B10}$$

Redefining the comoving distance as $\chi' = \chi/(H_0 R^{-1} c^{-1})$ for simplicity,

$$\frac{\partial \chi'}{\partial \lambda_i} = -\frac{1}{2} \int_0^z \frac{1}{E^3(z')} \frac{\partial \mathcal{E}(z')}{\partial \lambda_i} dz' \text{ for } \lambda_i \in (\Omega_m, \Omega_x, w_0, w_z). \tag{B11}$$

The dimensionless tangential comoving distance, $D'_M = (H_0/c)D_M$, can then be expressed as

$$D'_M = \frac{1}{\sqrt{|\Omega_k|}} S_k \left(\sqrt{|\Omega_k|}\chi' \right) = \frac{1}{\sqrt{\Omega_k}} \sinh \left(\sqrt{\Omega_k}\chi' \right), \tag{B12}$$

therefore

$$\frac{\partial D'_M}{\partial \lambda_i} = -\frac{1}{2} \frac{1}{\Omega_k^{3/2}} \frac{\partial \Omega_k}{\partial \lambda_i} \sinh \left(\sqrt{\Omega_k}\chi' \right)$$
$$+ \frac{1}{\sqrt{\Omega_k}} \cosh \left(\sqrt{\Omega_k}\chi' \right) \left(\frac{1}{2} \frac{1}{\sqrt{\Omega_k}} \frac{\partial \Omega_k}{\partial \lambda_i} \chi' + \sqrt{\Omega_k} \frac{\partial \chi'}{\partial \lambda_i} \right) \tag{B13}$$

for w_0 and w_z parameters $\partial \Omega_k/\partial \lambda_i = 0$. Therefore,

$$\frac{\partial D'_M}{\partial \lambda_i} = \cosh \left(\sqrt{\Omega_k}\chi' \right) \frac{\partial \chi'}{\partial \lambda_i}. \tag{B14}$$

Since we are assuming a flat universe in our investigations, we can use the Taylor expansions

$$\cosh(x) = 1 + x^2/2 + \dots$$

$$\sinh(x) = x + x^3/6 + \dots$$

therefore

$$\lim_{\Omega_k \to 0} \frac{\partial D'_M}{\partial \lambda_i} = \frac{\partial \chi'}{\partial \lambda_i} \text{ for } \lambda_i \in (w_0, w_z). \tag{B15}$$

For Ω_m and Ω_x parameters $\partial \Omega_k/\partial \lambda_i = -1$, therefore,

$$\frac{\partial D'_M}{\partial \lambda_i} = \frac{1}{2} \frac{1}{\Omega_k^{3/2}} \sinh \left(\sqrt{\Omega_k}\chi' \right) + \frac{1}{\sqrt{\Omega_k}} \cosh \left(\sqrt{\Omega_k}\chi' \right)$$
$$\times \left(-\frac{1}{2} \frac{1}{\sqrt{\Omega_k}} \chi' + \sqrt{\Omega_k} \frac{\partial \chi'}{\partial \lambda_i} \right). \tag{B16}$$

Once again substituting in the Taylor expansion

$$\lim_{\Omega_k \to 0} \frac{\partial D'_M}{\partial \lambda_i} = \frac{\partial \chi'}{\partial \lambda_i} - \frac{\chi'^3}{6} \text{ for } \lambda_i \in (\Omega_m, \Omega_x). \tag{B17}$$

The solutions above were given in Bassett et al. (2011), but are shown here for completeness.

B1 Derivatives of observables

For the analysis of SNe and HzSCs, we measure the distance modulus, so

$$\frac{\partial \mu}{\partial \lambda_i} = \frac{5}{D_L \ln(10)} \frac{\partial D_L}{\partial \lambda_i} = \frac{5}{D'_M \ln(10)} \frac{\partial D'_M}{\partial \lambda_i}. \tag{B18}$$

It is simple to then substitute this into Equation 4.

For BAO, we consider the parameters d_z and A. Therefore, the derivatives of importance are

$$\frac{\partial A}{\partial \lambda_i} = \frac{\sqrt{\Omega_m}}{z} \frac{\partial D'_V}{\partial \lambda_i} + \frac{D'_V}{2z\sqrt{\Omega_m}} \frac{\partial \Omega_m}{\partial \lambda_i}, \tag{B19}$$

where $D'_V = (H_0/c)D_V$ and

$$\frac{\partial D_V}{\partial \lambda_i} = \frac{D'_V}{3} \left(-\frac{1}{2E(z)^2} \frac{\partial \mathcal{E}(z)}{\partial \lambda_i} + \frac{2}{D'_M} \frac{\partial D'_M}{\partial \lambda_i} \right), \tag{B20}$$

and also

$$\frac{\partial d_z}{\partial \lambda_i} = \frac{1}{D_V} \frac{\partial r_s}{\partial \lambda_i} - \frac{r_s}{D_V^2} \frac{\partial D_V}{\partial \lambda_i} + \frac{\partial D_V}{\partial z_d} \frac{\partial z_d}{\partial \lambda_i}, \tag{B21}$$

where

$$\frac{\partial r_s}{\partial \lambda_i} = -\frac{c}{2\sqrt{3}H_0} \int_0^a \frac{da}{a^2\sqrt{1 + (3\Omega_b/4\Omega_\gamma)a}} \frac{1}{E^3} \frac{\partial \mathcal{E}}{\partial \lambda_i}. \tag{B22}$$

For the CMB, we consider the parameters ℓ_A, $\mathcal{R}$, and z^*,

$$\frac{\partial \mathcal{R}}{\partial \lambda_i} = \sqrt{\Omega_m} \frac{\partial D'_M}{\partial \lambda_i} + \frac{D'_M}{2\sqrt{\Omega_m}} \frac{\partial \Omega_m}{\partial \lambda_i} + \frac{\partial r_s}{\partial z^*} \frac{\partial z^*}{\partial \lambda_i} \tag{B23}$$

$$\frac{\partial \ell_A}{\partial \lambda_i} = \pi \left(-\frac{D'_M}{r_s(z_*)^2} \frac{\partial r_s(z_*)}{\partial \lambda} + \frac{1}{r_s(z_*)} \frac{\partial D'_M}{\partial \lambda} + \frac{\partial \ell_A}{\partial z^*} \frac{\partial z^*}{\partial \lambda_i} \right). \tag{B24}$$

We have omitted the explicit derivatives for $\partial \ell_A/\partial z^*$, $\partial z^*/\partial \lambda_i$, as they are trivial to calculate. The Fisher Matrix method is only used to determine the dark energy equation-of-state parameters constraints for the linear (CPL) parametrization.

APPENDIX C: SUPERNOVA-FITTING PROCEDURE AND COLOUR-STRETCH CORRECTION

SN measurements have an added complexity of a 'colour-stretch correction' in the determination of their magnitude calculation. The expected magnitude of the SNe is then taken to be

$$m_B = 5\log_{10} D_L(\mathcal{P}, z_{\text{cmb}}, z_{\text{hel}}) - \alpha(s-1) + \beta\mathcal{C} + M_B, \qquad \text{(C1)}$$

where z_{cmb} is the CMB frame redshift, z_{hel} is the heliocentric redshift, s is the stretch parameter, $\mathcal{C}$ is the colour parameter, and α and β parametrize the s–luminosity and $\mathcal{C}$–luminosity relationships. In this work, we substitute μ with m_B for the supernova analysis and marginalize over M_B.

The SNLS uses a combination of two light-curve-fitting software packages, SALT2 and SiFTO, to determine the stretch and colour parameters. They give equal weight to the fit parameters determined from each of the two software packages and include the difference between the results from each package in their systematic uncertainty budget. To fit the data in $w(z)$ analysis, we have marginalized over the stretch and colour parameters. The low-mass ($M_{\text{stellar}} \leq 10^{10} M_\odot$) and high-mass ($M_{\text{stellar}} > 10^{10} M_\odot$) host galaxy populations are fitted separately, as prescribed by Conley et al. (2011). In the Hubble parameter and dark energy density function fitting, we set the colour and stretch parameters to constant values of $\alpha = 1.45$ and $\beta = 3.16$. These values correspond to the best-fitting values found by Conley et al. (2011) for a flat wCDM model when only considering statistical error. Incorrect fitting of the stretch and colour parameters can cause cosmological discrepancies (Conley et al. 2011).

The covariance matrix is a combination of a systematics covariance matrix, and two covariance matrices which contain statistical errors in the SN model used in the light-curve fit. This follows the procedure outlined in Conley et al. (2011).

APPENDIX D: HUBBLE PARAMETER MEASUREMENTS

Existing Hubble parameter measurements from various sources (Simon et al. 2005; Stern et al. 2010; Blake et al. 2012; Chuang & Wang 2012; Moresco et al. 2012; Zhang et al. 2012; Busca et al. 2013) are given in Table D1. These measurements use different probes. The majority of the measurements come from relative age measurements of galaxies at different redshifts, using a variety of techniques, to infer the Hubble parameter (Simon et al. 2005; Stern et al. 2010; Moresco et al. 2012; Zhang et al. 2012). The relative age measurements are used as an estimator for dz/dt, which in turn gives $H(z)$. Simon et al. (2005) use observations of passively evolving galaxies and synthetic stellar population models to constrain the age of the oldest stars in the galaxy. Moresco et al. (2012) consider the 4000Å break (D4000) as a function of redshift and use stellar population synthesis models to theoretically calibrate the dependence of the differential age evolution on the differential D4000. Zhang et al. (2012) look at the evolution of luminous red galaxies (LRG), while Stern et al. (2010) consider how red-envelope galaxies evolve with time. The Hubble parameter estimates from Chuang & Wang (2012), Blake et al. (2012), and Busca et al. (2013) are determined from BAO scale measurements, sometimes in conjunction with other measurements, such as an Alcock–Paczynski

Table D1. Hubble parameter versus redshift from various sources and their corresponding analysis techniques, as described in Appendix D.

z	$H(z)$ (km s^{-1} Mpc^{-1})	σ_H (km s^{-1} Mpc^{-1})	Method	Reference
0.07	69	19.6	LRG−Age−z	Zhang et al. (2012)
0.1	69	12	Age−z+SNe	Simon et al. (2005)
0.12	68.6	26.2	LRG−Age−z	Zhang et al. (2012)
0.17	83	8	Age−z+SNe	Simon et al. (2005)
0.179	75	4	D4000−Age−z	Moresco et al. (2012)
0.199	75	5	D4000−Age−z	Moresco et al. (2012)
0.2	72.9	29.6	LRG−Age−z	Zhang et al. (2012)
0.27	77	14	Age−z+SNe	Simon et al. (2005)
0.28	88.8	36.6	LRG−Age−z	Zhang et al. (2012)
0.35	82.1	5	BAO	Chuang & Wang (2012)
0.352	83	14	D4000−Age−z	Moresco et al. (2012)
0.4	95	17	Age−z+SNe	Simon et al. (2005)
0.44	82.6	7.8	BAO +AP	Blake et al. (2012)
0.48	97	62	Red Envelope Galaxies: Age−z	Stern et al. (2010)
0.593	104	13	D4000−Age−z	Moresco et al. (2012)
0.6	87.9	6.1	BAO +AP	Blake et al. (2012)
0.68	92	8	D4000−Age−z	Moresco et al. (2012)
0.73	97.3	7	BAO+AP	Blake et al. (2012)
0.781	105	12	D400−Age−z	Moresco et al. (2012)
0.875	125	17	D4000−Age−z	Moresco et al. (2012)
0.88	90	40	Red Envelope Galaxies: Age−z	Stern et al. (2010)
0.9	117	23	Age−z+SNe	Simon et al. (2005)
1.037	154	20	D4000−Age−z	Moresco et al. (2012)
1.3	168	17	Age−z+SNe	Simon et al. (2005)
1.43	177	18	Age−z+SNe	Simon et al. (2005)
1.53	140	14	Age−z+SNe	Simon et al. (2005)
1.75	202	40	Age−z+SNe	Simon et al. (2005)
2.3	224	8	BAO+WMAP7	Busca et al. (2013)

measurement (Blake et al. 2012) or CMB measurements (Busca et al. 2013).

APPENDIX E: FISHER MATRIX METHOD

The fisher matrix analysis is a very popular method of predicting the capabilities of future surveys, and we have used this method throughout our analysis for computational simplicity. Despite its popularity, the Fisher Matrix method has come under some criticism in previous studies (Wolz et al. 2012; Khedekar & Majumdar 2013), as it only considers Gaussian errors in the parameter space, and therefore cannot accurately estimate asymmetric likelihood distributions. This means that Fisher analyses can reach 'forbidden' regions, and cannot completely trace degeneracies in the data that exist in reality. Its applicability also depends strongly on the stability of the derivatives of the likelihood and parameters. If the derivatives are unstable near the chosen model, the Fisher matrix will not be able to accurately represent this behaviour. However, when the constraints from all the probes are combined, the $w_0 - w_z$ contours are reasonably Gaussian and the Fisher matrix method can be used to predict the constraints on these parameters quite accurately. When we tested the validity of the Fisher matrix method compared to the χ^2 analysis, we generally found an agreement between the two methods to within 10 per cent.

This paper has been typeset from a TEX/LATEX file prepared by the author.